AMERICAN METEOROLOGICAL SOCIETY

Journal of Climate

EARLY ONLINE RELEASE

The DOI for this manuscript is doi: 10.1175/JCLI-D-17-0775.1

Global assessment of the Standardized Evapotranspiration Deficit Index (SEDI) for drought analysis and monitoring

Sergio M. Vicente-Serrano [1,*], Diego G. Miralles [2], Fernando Domínguez-Castro [1], Cesar Azorin-Molina [3], Ahmed El Kenawy [1,4], Tim R. McVicar [5,6], Miquel Tomás-Burguera [7], Santiago Beguería [7], Marco Maneta [8], Marina Peña-Gallardo [1]

Family names (or surnames) are underlined

[1] Instituto Pirenaico de Ecología, Spanish National Research Council (IPE-CSIC), Campus de Aula Dei, P.O. Box 13034, E-50059 Zaragoza, Spain; [2] Ghent University, Ghent, Belgium; [3] Regional Climate Group, Department of Earth Sciences, University of Gothenburg, Gothenburg, Sweden; [4] Department of Geography, Mansoura University, 35516, Mansoura, Egypt; [5] CSIRO Land and Water, Canberra, ACT, Australia; [6] Australian Research Council Centre of Excellence for Climate System Science, University of New South Wales, Sydney, Australia; [7] Estación Experimental de Aula Dei, Spanish National Research Council (EEAD-CSIC), Zaragoza, Spain; [8] Department of Geosciences, University of Montana, Missoula, MT, USA.

* Corresponding author: Sergio M. Vicente-Serrano (e-mail: svicen@ipe.csic.es)

Abstract. This article developed and implemented a new methodology for calculating the Standardized Evapotranspiration Deficit Index (SEDI) globally based on the log-logistic distribution to fit the evaporation deficit (ED), the difference between actual evapotranspiration (ETa) and atmospheric evaporative demand (AED). Our findings demonstrate that, regardless of the AED dataset used, a log-logistic distribution most optimally fitted the ED time series. As such, in many regions across the terrestrial globe, the SEDI is insensitive to the AED method used for calculation, with the exception of winter months and boreal regions. The SEDI showed significant correlations ($p < 0.05$) with the Standardized Precipitation Evapotranspiration Index (SPEI) across a wide range of regions, particularly for short (< 3-months) SPEI time-scales. This work provides a robust approach for calculating spatially and temporally comparable SEDI estimates, regardless of the climate region and land surface conditions, and it assesses the performance and the applicability of the SEDI to quantify drought severity across varying crop and natural vegetation areas.

Keywords: Drought, Evapotranspiration deficit, Log-logistic distribution, Evapotranspiration, SPEI.

1. Introduction

Drought is usually considered as a period of abnormally low water supply that fails to satisfy the existing demands of different natural systems and socioeconomic sectors. This situation is usually caused by a prolonged period of below average precipitation. It is well-known that drought is difficult to identify and quantify over space and time, which makes it one of the most complex natural hazards (Wilhite 1993, 2000; Vicente-Serrano 2016). This is particularly so because according to most definitions of drought, with the exception of those that focus exclusively on meteorological aspects, droughts are impact-dependent phenomena that affect a diverse range of natural and socioeconomic variables (Lloyd-Hughes 2014; Van Loon, 2015). Moreover, the degree of vulnerability and the capacity of recovery to drought occurrence strongly differ among regions as a function of their background socioeconomic and environmental characteristics (Simelton et al. 2009; Choat et al. 2012; Antwi-Agyei et al. 2012; Yang et al., 2017). Therefore, drought severity depends on meteorological conditions (e.g. magnitude and duration of precipitation shortage), and is also impacted by several human and environmental factors, such as land use or risk management (Van Loon et al. 2016).

However, the quantification of drought severity based on its impacts is a challenge, given the spatial differences, the sector of interest, as well as the availability of impact data (Stahl et al. 2015 and 2016). For these reasons, scientists, managers and policy makers usually quantify drought based on climate information only (McKee et al. 1993; Vicente-Serrano et al. 2010): the most widely-used drought metrics are generally based on climate information available across the globe. Overall, the potential of drought indices is particularly related to the possibility of quantifying drought severity and comparing their climate component both

58 spatially and temporally. A detailed review of current climate drought indices can be found in
59 Heim (2002), Keyantash and Dracup (2002) and Mishra and Singh (2010).
60
61 Being inexpensively and widely observed, precipitation is usually employed as the key input
62 variable in traditional drought indices (e.g. Palmer 1965; McKee et al. 1993). However,
63 precipitation is only one of the multiple variables that control water stress conditions in
64 natural ecosystems and affect water availability in usable water stores (e.g. soil moisture,
65 streamflow, reservoir storage, lake water). Water shortage is ultimately dependent on the
66 input of water through precipitation, lateral inflows, melting or irrigation, and is also crucially
67 regulated by the atmospheric evaporative demand (AED), i.e. the potential of the lower
68 atmosphere to receive water via evapotranspiration from the abovementioned terrestrial water
69 stores. Under low soil moisture, rising AED rates further increases vegetation water stress
70 (e.g., Ciais et al. 2005; McDowell et al. 2008; Zampieri et al. 2009), causing stomata closure
71 and the collapse of the photosynthetic machinery potentially resulting in crop failure (Lobell
72 et al. 2011; Asseng et al. 2015) and forest decay and mortality (Allen et al. 2015; Anderegg et
73 al. 2013; Breshears et al. 2013).
74
75 Numerous studies have demonstrated the importance of AED in triggering drought or
76 intensifying drought severity (e.g. Ciais et al. 2005; Otkin et al. 2016). For these reasons,
77 several drought indices use AED in their formulations. For example, compared to
78 precipitation-based drought indices, such as the Standardized Precipitation Index (SPI)
79 (McKee et al. 1993), the Standardized Precipitation Evapotranspiration Index (SPEI)
80 (Vicente-Serrano et al. 2010), which is obtained by means the standardization of the
81 difference between precipitation and AED at different time-scales, has shown better
82 performance in terms of identifying drought impacts in a variety of drought-prone systems

and regions across the globe (Vicente-Serrano et al. 2012; McEvoy et al. 2012; Wang et al. 2016; Chen et al. 2016; Labudova et al. 2017). In fact, it has been suggested that the AED may be the single most useful variable to quantify drought severity (McEvoy et al. 2016a). Accordingly, drought indices based only on AED have been recently formulated under the premise that AED anomalies are strongly connected, via a complementary relationship, with precipitation, soil moisture and actual evapotranspiration (ETa) anomalies (Hobbins et al. 2016; McEvoy et al. 2016b).

Here, a conceptual distinction between AED and ETa must be established. There are different forms to determine AED, among them pan evaporation (the evaporation from a pan full of water), or crop reference evapotranspiration (ETo) (the ETa of a hypothetical unstressed alfalfa grassland of uniform height with a closed canopy so the soil is shaded), which can be compared spatially since it calculation only depends on meteorological inputs (Katerji and Rana 2011). Independent of the choice of these definitions, AED does not directly depend on the actual water storage in land, and it is thus different from the ETa, which is the volume of water that is actually evaporated directly from soil/water/vegetation surfaces and/or transpired from vegetation into the atmosphere. While there are no water constrains for evaporation under humid conditions, ETa is constrained mainly by soil water availability (and ultimately by precipitation) in dry environments (Budyko 1948). As such, the use of drought indices that account only for AED is inappropriate in regions with non-constraining soil moisture conditions, given that a positive AED anomaly cannot be representative of drought severity. In such regions, water stress conditions are likely better quantified considering both AED and ETa.

From agronomic and eco-physiological perspectives, the evaporation deficit (ED), defined as the difference between ETa and AED, is more relevant than considering ETa or AED separately. Regardless of the climate regime, high ED causes stomatal closure, thus a decrease in the photosynthetic activity, carbohydrate accumulation and net primary production (Leuning 1995; Brümer et al. 2012; Vicente-Serrano et al. 2015). If the ED is very high and wilting point is reached, plants may die due to vascular damage (Will et al. 2013, Anderegg et al. 2015). Under the aforementioned assumptions, the ED has been proposed for quantifying drought severity (Narasimhan and Srinivasan 2005; Yao et al. 2010; Anderson et al. 2011; Kim and Rhee 2016). Unlike AED, which can be calculated by means of relatively simple physically-based models (e.g. Penman 1948; Allen et al. 1998; Rotstayn et al. 2006), the calculation of ETa is subject to many sources of uncertainty. ETa depends on a wide range of factors, including, but not limited to, AED, soil water availability, soil characteristics, vegetation morphology, physiology and phenology, and the complex relationships existing between these factors (Morton 1983).

Recently, the availability of remote sensing data and surface-atmosphere models has allowed for the development of global ETa products (Allen et al. 2007; Fisher et al. 2008; Mu et al. 2011; Miralles et al. 2011; Zhang et al. 2016). Similarly, drought indices have been developed based on the ED, mainly to analyze natural vegetation and crop stress; for instance, Anderson et al. (2011), Yao et al. (2010) and Mu et al. (2011) developed different normalized drought indices (e.g. the Evapotranspiration Deficit Index [EDI] and the Evaporative Stress Index [ESI]) by means of observational meteorological data and space-based products to estimate ED. Following the same rationale, Kim and Rhee (2016) proposed the Standardized Evapotranspiration Deficit Index (SEDI) using ETa data estimated based on Bouchet's (1963) complementary hypothesis, and used an approach widely used to calculate a drought index

132 comparable spatially and temporally (e.g. the SPI and the SPEI). Here, we follow the same
133 nomenclature proposed by Kim and Rhee (2016) to refer to a standardized drought index
134 based on the ED.
135
136 It is expected that future improvements on ETa estimates based on remote sensing data and
137 model outputs will increase the use of ETa for analyzing and monitoring drought at large
138 scale (Fisher et al. 2017). Our definition of SEDI allows for a straightforward utilisation of
139 these estimates. Yet, it is necessary to develop robust statistical calculation procedures, and to
140 comprehensively evaluate the usefulness of this indicator in comparison to other available
141 drought indices.
142
143 Our overarching goal is to provide a metric using ED to quantify drought severity and make
144 robust spatial and seasonal comparisons. Our specific objectives are to: (i) find a robust
145 probability distribution to fit the ED series worldwide to calculate the SEDI; (ii) compare the
146 impact of different AED estimations on the SEDI; (iii) compare the SEDI time series at the
147 global scale with another widely used drought index that accounts for precipitation and AED,
148 namely the SPEI; and (iv) assess the skill of the SEDI in terms of determining vegetation
149 activity anomalies globally.
150
151 **2. Data**
152 **2.1. Actual evapotranspiration**
153 We used ETa estimates from the Global Land Evaporation Amsterdam Model (GLEAM) v3a.
154 Full details about the development and characteristics of this dataset are found in Miralles et
155 al. (2011) and Martens et al. (2017). GLEAM is a methodology dedicated to deriving
156 evaporation from satellite observations of its main drivers. Interception loss is independently

157 calculated using Gash's (1979) analytical model forced by observations of precipitation and
158 vegetation cover while the remaining evaporation components use Priestley and Taylor's
159 (1972) potential evaporation formulation constrained by a multiplicative stress factor. For
160 transpiration and soil evaporation, this stress factor is calculated based on the content of water
161 in vegetation (microwave vegetation optical depth) and root zone (multilayer soil model
162 driven by observations of precipitation and updated through assimilation of microwave
163 surface soil moisture).
164 Actual evaporation estimates from GLEAM have been validated against eddy covariance
165 towers worldwide and errors have been estimated base on triple collocation analysis. Miralles
166 et al. (2011) reported average correlations of 0.83 and 0.90 for daily and monthly estimates,
167 respectively, and an average RMSD of ~ 0.3 mm day^{-1} for in situ validations against 43 eddy
168 covariance towers. More recently, Martens et al. (2017) reported a mean correlation of 0.81–
169 0.86 based on 91 eddy-covariance towers. In addition, GLEAM output has shown a better
170 performance than other available evaporation datasets to close the water balance over a wide
171 range of hydrological catchments, a better agreement with the expectations from the Budyko
172 framework, and a good skill to partition evaporation fluxes into transpiration, interception and
173 bare soil evaporation (Michel et al., 2016; Miralles et al., 2016). GLEAM datasets are openly
174 available globally at daily temporal resolution and 0.25º spatial resolution for 1980–2016
175 (https://www.gleam.eu). Here, we aggregated the data to monthly, 0.5º resolution.
176

177 **2.2. Atmospheric evaporative demand and precipitation**

178 To assess the sensitivity of SEDI to different AED inputs two AED datasets were used: (i)
179 GLEAM v3a (Miralles et al. 2011; Martens et al. 2017); and (ii) Climate Research Unit
180 (CRU) TS v.3.24.01 (Harris et al. 2014). GLEAM calculates Priestley and Taylor (1972)
181 potential evapotranspiration (ETp), which is only forced by incoming radiation and air

182 temperature, and here are used as a proxy of AED. The CRU TS AED is estimated by Allen's
183 et al. (1998) FAO-56 ETo Penman–Monteith equation which is simplified by assuming
184 spatio-temporally constant wind speed (Harris et al. 2014). For the calculation of SPEI we
185 used the analogous CRU TS precipitation dataset.
186
187 **2.3. Global GIMMS NDVI**
188 To compare the SEDI spatiotemporal variability with the anomalies of vegetation activity that
189 could be related to drought severity conditions, a metric of vegetation activity based on
190 satellite data was used. For this purpose, we used the Normalized Difference Vegetation
191 Index (NDVI) (3g.v1) dataset developed by the Global Inventory Monitoring and Modeling
192 System (GIMMS) observed by AVHRR sensors on-board NOAA satellites (Pinzon and
193 Tucker 2014), which Beck et al. (2011) demonstrated was the optimal AVHRR-NDVI dataset
194 for time series analysis. The NDVI exhibits a strong relationship with vegetation parameters
195 such as green biomass (Tucker et al. 1983; Gutman 1991) and fractional vegetation cover
196 (Gillies et al. 1997; Duncan et al. 1993). NDVI has long been used to analyze drought impacts
197 on vegetation (Liu and Kogan 1996; Kogan 1997; McVicar and Jupp 1998; Ji and Peters
198 2003; Vicente-Serrano et al. 2013; Papagiannopoulou et al. 2017). The NDVI dataset is
199 monthly at 0.5º resolution over 1981–2014. To facilitate a direct comparison between the
200 NDVI and SEDI in both space and time, the NDVI series were standardized by fitting the
201 monthly NDVI series to a log-logistic distribution and the cumulative probabilities were
202 transformed to standardized units following the same approach used for the SPI and the SPEI
203 (Vicente-Serrano 2006; Vicente-Serrano et al. 2010).
204
205 **3. Methods**
206 **3.1. Calculation of the evapotranspiration deficit from the gridded global data**

207 Recall that we define the evapotranspiration deficit (ED) as ETa – AED. Two versions of
208 monthly ED were calculated; both used monthly GLEAM ETa estimates with AED
209 formulations from: (i) CRU TS v. 3.24.01 ETo; and (ii) GLEAM ETp. These calculations
210 were performed for the terrestrial globe excluding the warm desert areas and Antarctica /
211 Greenland where several methodological limitations exist (Fisher et al. 2010; Beguería et al.
212 2014). Supplementary Figures 1 illustrates the spatial averages and standard deviations of the
213 ED in representative months of the four seasons of the year and Supplementary Figure 2
214 shows the temporal evolution of the ED in some world regions.
215
216 **3.2. Assessment of different probability distributions to calculate the SEDI**
217 Eight probability distributions were tested (General Extreme Value, Log-logistic, Log-normal,
218 Pearson III, Generalized Pareto, Weibull, Normal, and Exponential) to transform ED values to
219 a standardized normal variable (SEDI). These statistical distributions have been widely used
220 to standardize numerous hydrological and meteorological variables (e.g. Vicente-Serrano et
221 al. 2012b; Stagge et al. 2016), being a common tool to calculate spatially and temporally
222 comparable drought indices using either precipitation, AED or both (e.g. McKee et al. 1993;
223 Vicente-Serrano et al. 2010; Ma et al. 2014; Hobbins et al. 2016). Unfortunately, no previous
224 studies have tested the goodness of these distributions to fit ED values. Since the use of
225 different probability distributions may produce substantial differences in the resulting drought
226 indices (e.g. Stage et al. 2015; Vicente-Serrano and Beguería 2016), we calculated 16
227 different global SEDI datasets, each one using one of the aforementioned probability
228 distributions and the two different AED datasets (CRU TS v. 3.24.01 and GLEAM).
229 Following Hosking (1990) the parameters of the distributions were calculated using unbiased
230 Probability Weighted Moments (UB-PWMs). Calculations were performed independently for
231 each ED monthly series to account for the strong seasonality of ED in the majority of the

232 world climates. Once the monthly ED series were fit to a probability distribution, cumulative
233 probabilities of the ED values were obtained and transformed to standardized units (SEDI).
234 For this purpose, the classical approach of Abramowitz and Stegun (1965) was used, which is
235 also used for calculating other drought indices such as the SPI and the SPEI.
236
237 Similar to the SPI handling of months with no precipitation, the calculation of ED also
238 considers the case of months with ED = 0.0 mm/month. This occurs when ETa equals AED.
239 In humid and cold regions this conditions can occur frequently during winter months, even at
240 monthly time scales, given that ETa tends to approach AED and there is adequate water
241 availability to satisfy ETa (due to low AED) of these regions at these times. To cope with zero
242 values we implemented Stagge et al.'s (2015) approach to calculate the SPI, which is based
243 on the 'centre of mass' of the zero distribution rather than the maximum probability.
244
245 The UB-PWMs calculation of each monthly ED series requires a minimum of three values
246 larger than zero in the entire multi-annual record. In large areas of the northern hemisphere
247 ED is likely to be zero during the winter months, which makes it impossible to define the
248 SEDI in these months and regions. Additionally, a SEDI calculation based on some of the
249 eight tested probability distributions is not possible in some cases because the parameters of
250 that specific distribution cannot be fitted to the ED data. Moreover, in a few cases, the origin
251 parameter of the distribution can be higher than the lowest observed ED values, indicating no
252 solution for the SEDI in these cases.
253
254 To assess the performance and robustness of the eight probability distributions used for the
255 calculation of the SEDI, we firstly calculated the percentage of monthly ED series that cannot
256 be fitted by each of them, and distributions with high percentages were discarded (usually >

50%, see Table 1). With the remaining distributions, the normality of the resulting SEDI series across the terrestrial globe at each 0.50 degree resolution pixel was tested. Stagge et al. (2015) applied the Shapiro–Wilks (SW) test to determine whether the standardized variable (i.e. the SEDI) follows a standard normal distribution. The advantage of this test is that the parameter values are known beforehand, and not computed from the input data. The *p*-values of the SW test for each of the monthly global SEDI series obtained with the eight probability distributions were calculated. A rejection rate of $p < 0.05$ (corresponding to 95% confidence level) was used to discriminate the SEDI series that follow a normal standard variable.

Nevertheless, as shown by Vicente-Serrano and Beguería (2016), it is difficult to define the 'best' candidate distribution to calculate a standardized drought index, as the application of the SW goodness-of-fit test to evaluate the goodness of a distribution is limited at the tails of the distribution which are the most relevant values for a drought index. For this reason, we also analyzed the frequencies of high and low SEDI values obtained by the eight probability distributions and compared the associated return periods.

3.3. Comparison between SEDI obtained from two different AED datasets and between SEDI and SPEI

SEDI calculated using the CRU and GLEAM AED datasets were compared by means of the per-pixel Pearson's correlation coefficient considering the different monthly series.

3.4. Comparison between SEDI and SPEI

The SPEI at time-scales ranging between 1 and 24 months was calculated using CRU monthly precipitation and GLEAM AED data for 1981–2014. For this purpose, a log-logistic distribution and UB-PWMs were used (see details in Vicente-Serrano et al. 2010; Beguería et al. 2014 and Vicente-Serrano and Beguería 2016). For each pixel, we calculated the SPEI

time-scale that had the highest correlation with the SEDI for the different monthly series. Regardless of the SPEI timescale, we also calculated the spatial distribution of the maximum correlation between SPEI and SEDI.

3.5. Assessing the skill of the SEDI and SPEI in identifying spatiotemporal anomalies of vegetation state

Finally, the relationship between the standardized NDVI (sNDVI) and the SEDI and SPEI using Pearson's correlation coefficients was calculated. As the global relationship between vegetation activity and drought is strongly dependent on the drought time scale (Vicente-Serrano et al. 2013), the correlation between the sNDVI and the SPEI was calculated at time-scales ranging between 1 and 24 months. Given the strong seasonality of vegetation, correlations were calculated independently for specific months of the year as well as for the monthly time series as a whole. Regardless of the timescale of the SPEI, we only retained the lag of maximum correlations and compared it spatially with the correlations obtained between sNDVI and SEDI.

4. Results

4.1. Assessment of probability distributions to calculate the SEDI at the global scale

Table 1 show the percentage of monthly series for which the SEDI could not be calculated based on GLEAM and CRU AED data for each of the eight probability distributions used for standardization. The log-normal and Weibull distributions showed a markedly high percentage of series (often exceeding 40% of the terrestrial land-surface) with no solution for the SEDI suggesting that they are least suited for SEDI calculation, so they were removed from further analyses. The remaining six distributions showed smaller percentages of cases for which no solution could be found, with Normal and Exponential being slightly better. Interestingly, there is a clear seasonal pattern in the ability of these six distributions to fit the

ED series, with better performance found between March and September, compared to the October to February period. In comparison to the GLEAM AED, the SEDI calculated using the CRU AED shows a lower percentage of cases with no solution for the SEDI fitting. This may be explained by the higher AED values found in the CRU dataset.

< Table 1 here please >

The Shapiro-Wilks normality test applied to the SEDI series computed using the six remaining distributions indicated a poor performance of the Generalized Pareto, Normal and Exponential distributions, which had large percentages (typically 50% to 90%) of monthly series for which the null hypothesis of normality was rejected (Table 2, for the GLEAM and CRU AED datasets respectively). The remaining three distributions had a lower percentage of rejections, with the log-Logistic distribution having the lowest overall. The results were similar with the two AED datasets considered, although the SEDI calculated with the CRU AED yielded worse results (i.e., a larger proportion of rejections). In both AED cases, there was a notable seasonality, with fewer rejections in the boreal summer (less than 10% for log-Logistic) and more in boreal winter (around 25%).

< Table 2 here please >

Dry events are located in the lower tail of distribution and it is important to discern departures from normality in this region, even though data located there may represent less than 2–3% of all data. Figure 1(a) shows the relationship between the return periods and raw SEDI values obtained from GLEAM AED using log-logistic and GEV distributions, with Figure 1(b) documenting similar for the log-logistic and Pearson-III distributions. The SEDI values

obtained with GEV and Pearson-III distributions show more extreme values in both tails than those obtained with the log-logistic. This translates to higher return periods and more extreme SEDI values with GEV and Pearson-III distributions in comparison to the log-logistic.

< Figure 1 here please >

The frequencies of high and low SEDI events using the GEV probability distribution for standardization are unrealistically high using a sample of 35 years The plots are truncated to 1 event in 500 cases, corresponding to ± 2.88 sigmas, but even longer return periods were obtained with the GEV. On the other hand, the log-logistic distribution provided more coherent return periods and less extreme SEDI values. The plots also show that differences found in the high-density region (±1.80 sigmas) between the different probability distributions have only a residual influence on the SEDI values. The results based on the CRU AED yielded similar results. This is clearly illustrated in Figure 2, which shows the frequency of values below -2.58 sigmas (which corresponds to a return period of 1 in 200 years) in each time series. As expected, the majority of series do not show values below the threshold, but lower percentages dominate for the log-logistic distribution. The SEDI series obtained with GEV and Pearson III distributions show higher percentage of very extreme values. Given the relatively short sample used here (1980–2014, with the start-date determined by when the satellite remote sensing first become available), it is unlikely to find such a high frequency of SEDI cases corresponding to a return period higher than 200 years. Considering these results altogether (i.e., Tables 1-2 and Figures 1-2), we recommend the use of the log-logistic distribution for computing the SEDI series across the globe.

< Figure 2 here please >

359

360 **4.2. Comparison of SEDI series from two different AED datasets**

361 The boxplots in Figure 3 summarize the per-pixel correlations between the SEDI series and
362 the GLEAM and CRU AED datasets. All calculations were computed independently for each
363 month for the 34 years, and for the entire monthly time series altogether. In general,
364 correlations were dominantly positive and statistically significant ($p < 0.05$), albeit being
365 generally higher for April and September inclusive. There is large variability in the boxplots,
366 especially during the Northern Hemisphere cold-season where Pearson's r value range from
367 maximum positive to maximum negative values. Nevertheless, with the exception of the
368 Northern Hemisphere cold season, the percentage of series showing significant correlations
369 across the globe was generally higher than 70%. Figure 4 depicts the spatial distribution of
370 correlations between both datasets annually and for the mid-season months (i.e., January,
371 April, July and October). Results reveal markedly seasonal differences. During the boreal
372 winter (i.e., January), large areas of the Northern Hemisphere were not considered, given that
373 the SEDI had no solution for this region in the majority of the cases, as discussed in the
374 methods section. Nevertheless, in low latitudes, there were noticeable spatial differences in
375 the correlations. Although the latter were high in the majority of tropical and subtropical
376 regions, they were close to zero in the equatorial humid regions. This pattern persists in all
377 seasons, and all months. Overall, during the boreal spring (i.e., April) and summer (i.e., July),
378 large regions showed statistically significant correlations between the SEDI calculated using
379 AED from CRU and GLEAM.

380

381 < Figure 3 here please >

382 < Figure 4 here please >

383

384 The analysis of selected drought events illustrates a good agreement between the two datasets.
385 Figure 5 shows two recent exceptional droughts: (i) Russia (2010); and (ii) southern United
386 States/northern Mexico (2011). In both events, although there are some spatial differences in
387 the beginning and end of the drought periods, strong spatial agreement was exhibited between
388 the two SEDI datasets during the months of maximum extension of drought severity (July and
389 August for Russia and June-August for south North America).
390
391 < Figure 5 here please >
392
393 **4.3. Comparison of the SEDI and the SPEI at different time scales**
394 To avoid redundancy in the presentation of the results, in the following we only use the SEDI
395 series obtained with the GLEAM AED dataset and the log-logistic standardisation. The
396 temporal variability of the SEDI showed a strong agreement with the SPEI. Considering only
397 the SPEI time scale with the best correlation with the SEDI, large areas exhibited significant
398 correlation ($p < 0.05$) between both indices (Figure 6). For instance, in the boreal summer,
399 more than 85% of the world exhibited significant correlations between the SEDI and SPEI,
400 albeit the exceptionally low correlation in the rainforests of Amazonia, Congo and Southeast
401 Asia (Figure 7). In general, the globe's semi-arid regions showed the strongest (typically >
402 0.7) significant correlations between both drought indices, likely reflecting the ample seasonal
403 cycle and multi-annual climate variability in these regions.
404
405 < Figure 6 here please >
406 < Figure 7 here please >
407

SEDI series exhibited higher correlations with short SPEI time scales (Figure 8). Independent of the month, correlations were significant ($p < 0.05$) over the majority of globe, considering SPEI time scales between 1 and 9 months. With respect to longer time scales, the magnitude and statistical significance of the correlations diminished progressively. In the boreal summer, the differences in the magnitude of the correlations among the different time scales were lower, however lower correlations were observed for long SPEI time scales. About 40% of the world revealed the strongest correlation at the 1-month SPEI timescale, compared to 15–20% at the 2-month time scale (Table 3). In summary, around 80% of world exhibited the highest and most statistically significant ($p < 0.05$) correlations between the SEDI and SPEI considering SPEI time scales shorter than 5 months. Exceptionally, a few regions (< 10% of the terrestrial globe) showed the highest and most significant correlations at time scales longer than 9 months. Thus, during the boreal winter, apart from some areas in South America and central Africa, and in north latitudinal areas, the majority of regions showed maximum correlation between the SEDI and SPEI at short SPEI time scales (Figure 9). The areas that did not show significant correlations between the SEDI and SPEI mostly corresponded to those showing higher correlations at longer time scales (> 12 months). This finding demonstrates that where the SEDI is significantly correlated with SPEI, this correlation is recorded at short SPEI timescales (> 5 months).

< Table 3 here please >

< Figure 8 here please >

< Figure 9 here please >

4.4. Relationship between the SEDI, SPEI and the sNDVI

Figure 10 illustrates the spatial distribution of the correlations between the SEDI and sNDVI and between SPEI and sNDVI for mid-season months and for the entire record. There were important spatial differences in the magnitude of the correlations between the sNDVI and both drought indices at the global scale. Regardless of the month, higher and statistically significant correlations were found over semiarid regions, including – among others – southwestern North America, the Sahel, South Africa, Australia, and northeastern Brazil. Strong seasonality in the correlations related to the phenological cycles of vegetation was found. Monthly crossplots of SEDI and SPEI and their correlations with sNDVI are seen Figure 11, which illustrates that the spatial correlations were positive and statistically significant during all months. The correlations with sNDVI were higher for SPEI than for SEDI, particularly in the boreal summer (i.e., JJA).

< Figure 10 here please >

< Figure 11 here please >

The percentage of the terrestrial globe that showed significant correlations between either SEDI and sNDVI or SPEI and sNDVI were relatively small (typically ~15-45%; see Table 4. For the full monthly time series, less than 20% of the area exhibited significant correlations, independent of the selected drought index. This low percentage is partly explained by the fact that most ecosystems on Earth are not driven by water availability during one or more periods of the year (e.g., dormancy). Monthly correlations between the sNDVI and SPEI were statistically significant over more than 40% of the area during the boreal summer, where vegetation is active in large areas of the Northern Hemisphere. The SEDI showed lower percentages, with roughly 25% of the area showing significant correlations with the sNDVI during the same season.

457

458 < Table 4 here please >

459

460 **5. Discussion**

461 **5.1 Data used in the computation of the drought index**

462 In this study we delve into the computation and performance of the standardized
463 evapotranspiration deficit index (SEDI). The SEDI is based on the evapotranspiration deficit
464 (ED), which is defined as the difference between the actual evapotranspiration (ETa) and the
465 atmospheric evaporative demand (AED). The rationale behind this computation is to
466 explicitly account for the water actually used by the vegetation (the ETa) compared with the
467 amount of water that the same ecosystem would have used in an ideal perfect hydric state, i.e.
468 with no water stress. The departures between ETa and AED allow quantification of the degree
469 of water stress the vegetation is suffering, i.e. the drought state. Nevertheless, it is also
470 necessary to state that ED defined here may depend on many other factors (e.g., leaf-out
471 period, harvesting, fire, pests) and not just water availability.

472 A major technical problem with this approach is how to obtain values of both ETa and AED,
473 most notably the former. The recent availability of global ETa datasets based on satellite
474 observations (McCabe et al. 2016; Miralles et al. 2016; Zhang et al. 2016), however, has
475 opened the possibility to explore this approach.

476 Several studies have already proposed the quantification of drought severity based on either
477 the ED, the ratio between ETa and AED, or using ETa estimations obtained from remote
478 sensing data (e.g. Yao et al. 2010; Anderson et al. 2011). In their South Korean study, Kim
479 and Rhee (2016) proposed the use of the ED to develop a drought index. They estimated ETa
480 following the Budyko theoretical approach, which establishes a non-linear relationship
481 between the AED/Precipitation ratio and the ETa/Precipitation ratio. The novelty of our study

482 is that it calculates the SEDI globally, using ETa from a global satellite dataset (GLEAM).
483 Despite the uncertainties in GLEAM, its detailed description of the soil water balance and
484 phenological stress mean an improvement over using ETa estimations using Budyko's
485 hydroclimatic framework (Martens et al. 2017).
486 Regarding the AED data, two datasets were compared to calculate the SEDI globally. The
487 first (GLEAM) calculates AED using the Priestley and Taylor (1972) potential ET
488 formulation. The second (CRU) calculates AED using a simplification of Allen et al's (1998)
489 FAO-56 Penman-Monteith equation. Several studies have shown that the spatial and temporal
490 variability of the AED is strongly dependent on the methodology used to estimate this
491 variable (e.g. Espadafor et al. 2011; Vicente-Serrano et al. 2014; Wang et al. 2015; Fisher et
492 al. 2010), and on the uncertainty in the atmospheric forcing data (McVicar et al. 2012a,b).
493 Here, we assessed the sensitivity of the global-scale SEDI to the choice of AED, and found
494 notable differences in the boreal winter months (i.e., DJF) and also in the humid equatorial
495 regions during their summer months (i.e., JJA) – these are regions in which the aerodynamic
496 component of AED can be substantial (McVicar et al. 2012b). As Priestley and Taylor is a
497 radiative based estimate of ETp (Donohue et al. 2010) which does not include aerodynamic
498 variables (i.e., relative humidity) explicitly in its calculations, whereas the FAO-56 Penman-
499 Monteith formulation does, they are expected to depart. Conversely, in sub-humid to semi-
500 arid climates of both hemispheres, and especially during their summer, the correlation
501 between the two SEDI datasets was strong and not sensitive to the AED dataset used in the
502 calculations. This is highly relevant for drought analysis and monitoring since in these regions
503 vegetation dynamics are more determined by drought variability (Vicente-Serrano et al.
504 2013).
505 In tropical forests, the correlation between both SEDI datasets was statistically not significant,
506 regardless of the season of the year. There are several factors driving this pattern. It can be

507 related to the low climate data availability. While GLEAM AED uses reanalysis output the
508 CRU AED depends on observational data, which are sparse over these regions (Harris et al.
509 2014). It can also be related to uncertainties in the reanalysis output meteorological fields,
510 which are the likely cause for the difference found between the two SEDI datasets,
511 particularly for those variables that are most difficult to model such as wind speed and solar
512 radiation (McVicar et al. 2008; Perdigao et al. 2016). Moreover, the lack of relative humidity
513 in the Priestley and Taylor scheme could affect the estimations, given that strong changes in
514 this variable have been recorded in observations and reanalysis output over the past two
515 decades (Willett et al. 2014; Vicente-Serrano et al. 2017) and it is taken into account in the
516 Penman-Monteith ETo.
517 Despite the differences found, the SEDI provides a quantification of the intensity of drought
518 that is largely independent of the method used to compute the AED in most global regions
519 affected by recurrent droughts events. Low sensitivity of the SEDI to the methodology used to
520 estimate AED is relevant for the evaluation of impact in some regions such as the Sahel,
521 South America, or central Asia. In these regions the impacts of droughts are usually severe
522 and quantifying the extent and intensity of drought conditions is critical to inform policy and
523 guide mitigating action.
524 Although we provide an initial assessment of the impact of using different datasets to
525 compute the SEDI at globally, further research is needed to test the sensibility of the SEDI to
526 both ETa and AED variables under a range of climate and land-cover conditions, and to
527 investigate the impact of using different ETa and AED datasets in the calculation of the SEDI.
528 Meanwhile, there are several international initiatives to improve the quality and assess the
529 uncertainties in global ET data from satellite and in situ observations (Zhang et al. 2016;
530 McCabe et al. 2017; Fisher et al. 2017).
531

5.2. Optimum probability distribution to calculate the SEDI worldwide

This study tested eight standardizing probability distributions approaches calculate the SEDI, and proposed a robust methodology to obtain global SEDI values that are spatially and temporally comparable. The log-logistic probability distribution showed clear advantages for calculating the SEDI. This distribution has already been recommended when calculating the SPEI (Vicente-Serrano et al. 2010; Vicente-Serrano and Beguería 2016). From the tested distributions, only the GEV, Pearson-III and log-logistic distributions provided solutions for the SEDI over most of the terrestrial globe, and provided SEDI series that most frequently followed a standard normal distribution. The Pearson-III distribution has been proposed to calculate the SPI (Guttman 1999; Vicente-Serrano 2006) as the most reliable alternative to the original proposed standardization using the Gamma distribution (McKee et al. 1993). However, here we found that the Pearson-III distribution yielded a higher number of SEDI series that did not follow a normal distribution compared to the log-logistic distribution. Moreover, the Pearson-III distribution tended to overestimate the frequency of extreme SEDI values at both ends of the distribution. The same was found with the GEV distribution, proposed by Stagge et al. (2015) for calculating the SPEI. Based on our global results we recommend the use of the log-logistic distribution to fit monthly ED series across the terrestrial environment to obtain the SEDI. Moreover, this recommendation holds independently of the AED form used in this study.

5.3. Comparison of the SEDI with the SPEI

The SPEI has been thoroughly validated and used to detect and monitor moisture anomalies for agricultural (e.g. Zipper et al. 2016; Wang et al. 2016; Pascoa et al. 2017) and environmental applications (e.g. Zhang et al. 2017; Greenwood et al. 2017). The SEDI showed positive significant correlations with the SPEI over most terrestrial ecosystems, with

557 some exceptions in the equatorial region and across some boreal regions. Under abundant soil
558 moisture the SPEI could also show a drought signal if precipitation is below average when
559 really there is limited plant available soil water constrain. This suggests that in some areas
560 SPEI and SEDI are complementary. In areas in which the ETa strongly depends on
561 precipitation (e.g., arid and semi-arid regions) SPEI and SEDI are expected to fit well; in
562 other regions they could provide different but complementary information to assess drought
563 severity. Nonetheless, during the summer boreal season, the SEDI showed significant
564 correlation with the SPEI over the entire Northern Hemisphere. If all data was perfect, SEDI
565 would be better in capturing vegetation impacts simply because the use of precipitation in
566 SPEI is meant to be as a surrogate for plant water availability. Thus, SPEI uses precipitation
567 as proxy of ETa to identify drought impacts on vegetation. This approach, although less
568 consistent physically than the SEDI, may produce better results to determine drought severity
569 than a complex physical simulation model (i.e., Vicente-Serrano et al. 2011).
570 The SEDI was best correlated with the SPEI at short time scales, with the highest and most
571 significant correlations recorded at 1- and 2-month time scales, independent of the month.
572 There are a few regions where the strongest correlations between the SPEI and SEDI were
573 observed at time scales longer than 18 months, but these correlations were not statistically
574 significant. Therefore, we can regard SEDI as a short time scale drought index, characterized
575 by its sensitivity to high frequency climate variations. Kim and Rhee (2016) suggested the
576 calculation of the SEDI at a timescale of 9 months by standardizing the cumulative ET and
577 AED differences over the previous nine months. They justified the selection of this period by
578 the high correlation found between the Palmer Drought Severity Index (PDSI) and the SPEI at
579 this time scale (see Vicente-Serrano et al. 2010b). We showed that in most regions of the
580 world, the standardized anomalies of the ED are mostly determined by the high-frequency

581 variability of the climatic water balance recorded at short time scales, which makes
582 recommendable the use of the SEDI at 1-month timescale.
583 The selection of a specific time scale for drought analysis is justified by the different
584 characteristic response times of agricultural, hydrological and environmental systems to water
585 shortage. Water shortages are mostly determined by precipitation shortfalls (McKee et al.
586 1993) and/or increased AED (Vicente-Serrano et al. 2010). The use of different drought time
587 scales is essential to adjust the duration of anomalous climate conditions to the anomalous
588 response of the ecohydrologic system, such as abnormally low stream flows (e,g. López-
589 Moreno et al. 2013; Lorenzo-Lacruz et al. 2013; Barker et al. 2016; see further clarifications
590 and discussion on the drought time scales in Vicente-Serrano et al. 2011). However, the use of
591 long cumulative time scales is not justified for the SEDI because ED is mostly determined by
592 high-frequency variability in climatic conditions. In essence, this is similar to those
593 streamflow-based drought indices, such as the Standardized Streamflow Index (SSI, Vicente-
594 Serrano et al. 2012). For instance, like the SSI, the SEDI could also be considered a direct
595 indicator of the impact of droughts on vegetation because the AED is an important driver of
596 vegetation gross primary production through its control on plant stomatal closure and plant
597 respiration (Stephenson 1990, 1998) and because ETa strongly controls photosynthesis and
598 carbon uptake (Donohue et al. 2014; Yang et al. 2015).
599
600 **5.4. Performance of the SEDI to identify vegetation anomalies associated with drought**
601 The response of vegetation activity, measured as greenness indices (e.g. NDVI) from satellite
602 imagery, to water availability is complex. Numerous studies have demonstrated different
603 spatial and seasonal relationships between NDVI and different climate drought indices (e.g. Ji
604 and Peters 2003; Quiring and Paraprikaou 2008). Here, we demonstrated that the correlation
605 between the sNDVI and the SPEI and SEDI was strongly variable over both space and time.

606 As expected, a clear relationship was recorded in semi-arid regions, which in general show a
607 higher response to soil water availability, compared to sub-humid and humid regions in which
608 vegetation is driven by other climatic and environmental factors (Vicente-Serrano et al. 2013;
609 Papagiannopoul et al. 2017). Overall, a lower correlation of the sNDVI to the SEDI than to
610 the SPEI was found. In general, the correlations were higher and more frequently statistically
611 significant between the sNDVI and SPEI, possibly due to the higher flexibility of the SPEI,
612 which is computed at different time scales, since the relationship between vegetation activity
613 and drought indices strongly differs as a function of the timescale at which drought indices
614 were calculated (Pasho et al. 2011; Vicente-Serrano et al. 2013, 2015). SPEI would show
615 higher flexibility to compute water deficits recorded at different timescales since vegetation
616 types have several physiological strategies to cope with water stress (Chaves et al. 2003).
617 Thus, stomatal closure under high vapor pressure deficit conditions is a mechanism to reduce
618 water losses and hydrologic stress in plants. Although during periods of low transpiration
619 photosynthesis may be reduced, non-structural carbohydrates in the plant can maintain plant
620 metabolism and maintain greenness (Rosas et al. 2013).
621 Overall, we indicated that although the SEDI showed lower correlations, it exhibited similar
622 spatial patterns of correlation with the sNDVI. Compared to the SPEI, SEDI's sensitivity to
623 high-frequency changes in ED makes it more suitable for identifying regions where leaf
624 activity is highly sensitive to water stress conditions. We defend that using and combining
625 different drought indices is the best approach for drought quantification, analysis and
626 monitoring. The recently proposed SEDI based on the satellite-based ET data can
627 complement traditional drought indices and provide information about regions that are
628 sensitive to short-term changes in atmospheric demand. Figure 12 provides a representative
629 example of two exceptional drought events recorded in the Iberian Peninsula in 1995 and the
630 Sahel in 1984. In both cases, the SEDI and 3-month SPEI showed strong drought severity

631 over large areas and months, but they did not exactly agree either over space or in magnitude,
632 which indicates that SEDI is bringing new information not captured by the SPEI. NDVI
633 anomalies were different in time and space from each of the drought indices (SEDI and
634 SPEI), indicating that none of them alone captures the full impact on vegetation greenness,
635 with additional insight possible when both indices are combined.
636
637 < Figure 12 here please >
638
639 **6. Conclusion**
640 We provided recommendations on the best approaches for calculating a temporally and
641 spatially comparable SEDI, regardless of the climate region and land surface conditions.
642 Although the performance of the SEDI for monitoring the hydric status of ecosystems, and
643 despite its theoretical superiority since it is based on directly comparing the use of water
644 (ETa) with its theoretical demand (AED), we have shown that other indices such as the SPEI
645 which do not require estimation of the ETa showed a similar performance to identify drought
646 severity globally. In any case, SEDI calculations will benefit from further improvements in
647 remotely sensed ETa. Additionally, while the SEDI can be of interest for drought assessment
648 related to crops and natural vegetation, its potential application in relation to other drought
649 impacts such as river discharges, reservoir storages or groundwater levels is yet to be
650 explored. The SEDI global dataset developed in this study is available at
651 http://hdl.handle.net/10261/160091.
652
653 **Acknowledgements**
654 This work was supported by the research projects PCIN-2015-220 and CGL2014-52135-C03-
655 01 financed by the Spanish Commission of Science and Technology and FEDER,
656 IMDROFLOOD financed by the Water Works 2014 co-funded call of the European
657 Commission and INDECIS, which is part of ERA4CS, an ERA-NET initiated by JPI Climate,

and funded by FORMAS (SE), DLR (DE), BMWFW (AT), IFD (DK), MINECO (ES), ANR (FR) with co-funding by the European Union (Grant 690462). Diego G. Miralles acknowledges support from the European Research Council (ERC) under grant agreement n° 715254 (DRY–2–DRY). Marina Peña-Gallardo was granted by the Spanish Ministry of Economy and Competitiveness and Miquel Tomas-Burguera was supported by a doctoral grant by the Ministerio de Educación, Cultura y Deporte.

References

Abramowitz, M., and Stegun, I.A. 1965: *Handbook of Mathematical Functions*, Dover Publications, New York.

Allen, R.G., L.S. Pereira, D. Raes, and M. Smith. 1998: *Crop evapotranspiration: Guidelines for computing crop water requirements*. Food and Agricultural Organization (FAO), Irrig. Drain. pap. 56, Rome,

Allen, R.G., M. Tasumi, and R. Trezza. 2007: Satellite-based energy balance for mapping evapotranspiration with internalized calibration (METRIC) – Model. *Journal of Irrigation and Drainage Engineering*, **133**, 380-394.

Allen, C.D., D.D. Breshears, and N.G. McDowell. 2015: On underestimation of global vulnerability to tree mortality and forest die-off from hotter drought in the Anthropocene. *Ecosphere*, **6**, 129.

Anderegg, L.D.L., W.R.L. Anderegg, J. Abatzoglou, A.M. Hausladen, and J.A. Berry. 2013: Drought characteristics' role in widespread aspen forest mortality across Colorado, USA. *Global Change Biology*, **19**, 1526-1537.

Anderegg, W.R.L., A. Flint, C.-Y Huang, and Coauthors. 2015: Tree mortality predicted from drought-induced vascular damage. *Nature Geoscience*, **8**, 367–371.

Anderson, M.C., C. Hain, B. Wardlow, B. and Coauthors. 2011: Evaluation of drought indices based on Thermal remote sensing of evapotranspiration over the continental United States. *Journal of Climate*, **24**, 2025-2044.

Antwi-Agyei, P., E.D.G. Fraser, A.J. Dougill, L.C. Stringer, and E. Simelton. 2012: Mapping the vulnerability of crop production to drought in Ghana using rainfall, yield and socioeconomic data. *Applied Geography*, **32**, 324-334.

Asseng, S., F. Ewert, P. Martre, and Coauthors. 2015: Rising temperatures reduce global wheat production. *Nature Climate Change*, **5**, 143-147.

Barker, L.J., J. Hannaford, A. Chiverton, C. Svensson. 2016: From meteorological to hydrological drought using standardised indicators. *Hydrology and Earth System Sciences*, **20**, 2483-2505.

Beck, H.E., T.R. McVicar, A.I.J.M. van Dijk, J. Schellekens, R.A.M. de Jeu, and L.A. Bruijnzeel, 2011: Global evaluation of four AVHRR-NDVI data-sets: Intercomparison and assessment against Landsat imagery. *Remote Sensing of Environment*, **115**, 2547-2563.

Beguería, S., S.M. Vicente-Serrano, F. Reig, and B. Latorre. 2014: Standardized Precipitation Evapotranspiration Index (SPEI) revisited: parameter fitting, evapotranspiration models, kernel weighting, tools, datasets and drought monitoring. *International Journal of Climatology*, **34**, 3001–3023.

Breshears, D.D., Adams, H.D., Eamus, D. and Coauthors. 2013: The critical amplifying role of increasing atmospheric moisture demand on tree mortality and associated regional die-off. Frontiers in Plant Science 4(AUG),266

Brümmer, C., T.A. Black, and R.S. Jassal. 2012: How climate and vegetation type influence evapotranspiration and water use efficiency in Canadian forest, peatland and grassland ecosystems. *Agricultural and Forest Meteorology*, **153**, 14-30.

Bouchet, R.J. 1963: Evapotranspiration réelle evapotranspiration potentielle, signification climatique, 134–142, in International Association of Scientific Hydrology, General Assembly of Berkeley, Transactions, vol. 2, Evaporation, Berkeley, Calif

Budyko, M.I. 1948: Evaporation Under Natural Conditions, Gidrometeorizdat, Jerusalem.

Chaves, M.M., J.P. Maroco, and J.S. Pereira. 2003: Understanding plant responses to drought—From genes to the whole plant. *Funct Plant Biol*, **30**, 239–264.

Chen, T., G. Xia, T. Liu, W. Chen, and D. Chi. 2016: Assessment of drought impact on main cereal crops using a standardized precipitation evapotranspiration index in Liaoning Province, China. *Sustainability (Switzerland)*, **8**, art. no. 1069.

Choat, B., S. Jansen, T.J. Brodribb, and Coauthors. 2012: Global convergence in the vulnerability of forests to drought. *Nature,* **491**, 752-755.

Ciais Ph, and Coauthors. 2005: Europe-wide reduction in primary productivity caused by the heat and drought in 2003. *Nature*, **437**, 529–533.

Donohue, R.J., T.R. McVicar, and M.L. Roderick. 2010: Assessing the ability of potential evaporation formulations to capture the dynamics in evaporative demand within a changing climate. *Journal of Hydrology*, **386**, 186-197.

Donohue, R.J., I.H. Hume, M.L. Roderick, and Coauthors. 2014: Evaluation of the remote-sensing-based DIFFUSE model for estimating photosynthesis of vegetation. *Remote Sensing of Environment*, **155**, 349-364.

Duncan, J., D. Stow, J. Franklin, and A. Hope. 1993. Assessing the relationship between spectral vegetation indices and shrub cover in the Jordana Basin, New Mexico. *International Journal of Remote Sensing*, **14**, 3395–3416.

Espadafor, M., I. J. Lorite, P. Gavilán, and J. Berengena, 2011: An analysis of the tendency of reference evapotranspiration estimates and other climate variables during the last 45 years in southern Spain. Agric. *Water Manage.*, **98**, 1045–1061.

Fisher, J., K. Tu, and D. Baldocchi, 2008: Global estimates of the land-atmosphere water flux based on monthly AVHRR and ISLSCP-II data, validated at 16 FLUXNET sites. *Remote Sensing of Environment*, **112**, 901–919.

Fisher, J.B., R.J. Whittaker, and Y. Malhi, 2010: ET come home: potential evapotranspiration in geographical ecology. *Global Ecology and Biogeography*, **20**, 1–18.

Fisher, J. B., F. Melton, E. Middleton, C. Hain, and Coauthors. 2017: The future of evapotranspiration: Global requirements for ecosystem functioning, carbon and climate feedbacks, agricultural management, and water resources. *Water Resources Research*, **53**, 2618–2626.

Gash, J., 1979: An analytical model of rainfall interception by forests. *Quarterly Journal of the Royal Meteorological Society*, **105**, 43–55.

Gillies, R.R., T.N. Carlson, J. Cui, W.P. Kustas, and K.S. Humes. 1997: A verification of the triangle method for obtaining surface soil water content and energy fluxes from remote measurements of the Normalized Difference Vegetation Index (NDVI) and surface radiant temperature. *International Journal of Remote Sensing*, **18**, 3145–3166.

Greenwood, S., P. Ruiz-Benito, J. Martínez-Vilalta, and Coauthors. 2017: Tree mortality across biomes is promoted by drought intensity, lower wood density and higher specific leaf area. *Ecology Letters*, **20**, 539-553.

Gutman, G. 1991: Vegetation indices from AVHRR: an update and future prospects. *Remote Sensing of Environment*, **35**, 121–136.

Guttman, N.B. 1999: Accepting the standardized precipitation index: A calculation algorithm. *Journal of the American Water Resources Association*, **35**, 311–322.

Harris, I, P.D. Jones, T.J. Osborn, and D.H. Lister. 2014: Updated high-resolution grids of monthly climatic observations – the CRU TS3.10 dataset. *Int. J. Climatol.*, **34**, 623–642.

Heim, R.R. 2002: A review of twentieth-century drought indices used in the United States. *Bull. Amer. Meteor. Soc.*, **83**, 1149–1165.

Hobbins, M.T., A. Wood, D.J. McEvoy, D.J., and Coauthors. 2016: The evaporative demand drought index. Part I: Linking drought evolution to variations in evaporative demand. *Journal of Hydrometeorology*, **17**, 1745-1761.

Hosking, J.R.M. 1990: L-moments: Analysis and estimation of distributions using linear combinations of order statistics. *Journal of Royal Statistical Society B*, **52**, 105–124.

Ji, L., and Peters, A.J. 2003: Assessing vegetation response to drought in the northern Great Plains using vegetation and drought indices. *Remote Sensing of Environment*, **87**, 85-98.

Katerji, N., and Rana, G. 2011: Crop Reference Evapotranspiration: A Discussion of the Concept, Analysis of the Process and Validation. *Water Resources Management*, **25**, 1581-1600.

Keyantash, J., and J. Dracup. 2002: The quantification of drought: An evaluation of drought indices. *Bull. Amer. Meteor. Soc.*, **83**, 1167–1180.

Kim, D., and J. Rhee. 2016: A drought index based on actual evapotranspiration from the Bouchet hypothesis. *Geophysical Research Letters*, **43**, 10277-10285.

Kogan, F.N. 1997: Global drought watch from space. *Bulletin of the American Meteorological Society*, **78**, 621-636.

Labudova, L., M. Labuda, and A. Taka. 2017: Comparison of SPI and SPEI applicability for drought impact assessment on crop production in the Danubian Lowland and the East Slovakian Lowland. *Theoretical and Applied Climatology*, **128**, 491–506.

Leuning, A. 1995: A critical appraisal of a combined stomatal-photosynthesis model for C3 plants. *Plant, Cell and Environment*, **18**, 339-335.

Liu, W.T., and F.N. Kogan. 1996: Monitoring regional drought using the vegetation condition index. *International Journal of Remote Sensing*, **17**, 2761-2782.

Lloyd-Hughes, B. 2014: The impracticality of a universal drought definition. *Theoretical and Applied Climatology*, **117**, 607-611.

Lobell, D.B., M. Bänziger, C. Magorokosho, and B. Vivek. 2011: Nonlinear heat effects on African maize as evidenced by historical yield trials. *Nature Climate Change*, **1**, 42-45.

López-Moreno, J.I., S.M., Vicente-Serrano, J. Zabalza, S. Beguería, J. Lorenzo-Lacruz, C. Azorin-Molina, E. Morán-Tejeda. 2013: Hydrological response to climate variability at different time scales: a study in the Ebro basin. *Journal of Hydrology*, **477**, 175-188.

Lorenzo-Lacruz, J., S.M. Vicente-Serrano, J.C. González-Hidalgo, J.I. López-Moreno, N. Cortesi. 2013: Hydrological drought response to meteorological drought at various time scales in the Iberian Peninsula. *Climate Research*, **58**, 117-131

Ma, M., L. Ren, F. Yuan, and Coauthors. 2014: A new standardized Palmer drought index for hydro-meteorological use. *Hydrol. Process.*, **28**, 5645–5661.

Martens, B., D.G. Miralles, H. Lievens, and Coathors. 2017: GLEAM v3: satellite-based land evaporation and root-zone soil moisture. *Geoscientific Model Development*, **10**, 1903–1925.

McCabe, M.F., A. Ershadi, C. Jiménez, D.G. Miralles, D. Michel, E.F. Wood. 2016: The GEWEX LandFlux project: evaluation of model evaporation using tower-based and globally gridded forcing data. *Geoscientific Model Development*, **9**, 283–305.

McCabe, M.F., M. Rodell, D.E. Alsdorf, D.G. Miralles, R. Uijlenhoet, W. Wagner, W., and Coauthors. 2017: The Future of Earth Observation in Hydrology. *Hydrology and Earth System Sciences*, **21**, 3879–3914

McDowell, N., W.T. Pockman, W.T., C.D. Allen, and Coauthors. 2008: Mechanisms of plant survival and mortality during drought: Why do some plants survive while others succumb to drought? *New Phytologist*, **178**, 719-739.

McEvoy, D.J., J.L. Huntington, J.T. Abatzoglou, L.M. Edwards. 2012: An evaluation of multiscalar drought indices in Nevada and Eastern California. *Earth Interactions* **16**, https://doi.org/10.1175/2012EI000447.1

McEvoy, D.J., J.L. Huntington, J.F. Mejia, M.T. Hobbins. 2016a: Improved seasonal drought forecasts using reference evapotranspiration anomalies. *Geophysical Research Letters*, **43**, 377-385.

McEvoy, D.J., J.L. Huntington, M.T. Hobbins, and Coauthors. 2016: The evaporative demand drought index. Part II: CONUS-wide assessment against common drought indicators. *Journal of Hydrometeorology*, **17**, 1763-1779.

McKee, T.B.N., J. Doesken, and J. Kleist. 1993: The relationship of drought frequency and duration to time scales. Proc. Eight Conf. on Applied Climatology. Anaheim, CA, Amer. Meteor. Soc. 179–184.

McVicar, T.R., and D.L.B Jupp. 1998: The current and potential operational uses of remote sensing to aid decisions on Drought Exceptional Circumstances in Australia: A Review. *Agricultural Systems*, **57**, 399- 468.

McVicar, T.R., T.G. Van Niel, L.T. Li, and Coauthors. 2008: Wind speed climatology and trends for Australia, 1975-2006: Capturing the stilling phenomenon and comparison with near-surface reanalysis output. *Geophysical Research Letters*, **35**, L20403.

McVicar, T.R., M.L. Roderick, R.J. Donohue, and Van Niel, T.G. 2012a: Less bluster ahead? ecohydrological implications of global trends of terrestrial near-surface wind speeds. *Ecohydrology*, **5**, 381–388.

McVicar, T.R., M.L. Roderick, R.J. Donohue, and Coauthors. 2012b: Global review and synthesis of trends in observed terrestrial near-surface wind speeds: implications for evaporation. *J. Hydrol.*, **416–417**, 182–205.

Miralles, D. G., T.R.H. Holmes, R.A.M. De Jeu, J.H. Gash, A.G.C.A. Meesters, A.J. Dolman, 2011: Global land-surface evaporation estimated from satellite-based observations. *Hydrology and Earth System Sciences*, **15**, 453–469.

Miralles, D.G., C. Jiménez, M. Jung, D. Michel, and Coauthors, 2016: The WACMOS-ET project – Part 2: Evaluation of global terrestrial evaporation data sets. *Hydrology and Earth System Sciences*, **20**, 823–842.

Mishra, A.K., V.P Singh, V.P. 2010: A review of drought concepts. *J. Hydrol.*, **391**, 202–216.

Morton, F.I.1983: Operational estimates of areal evapotranspiration and their significance to the science and practice of hydrology. *Journal of Hydrology*, **66**, 1-76.

Mu, Q., M. Zhao, S.W. Running. 2011: Improvements to a MODIS global terrestrial evapotranspiration algorithm. *Remote Sensing of Environment*, **115**, 1781-1800.

Narasimhan, B. and R. Srinivasan. 2005: Development and evaluation of Soil Moisture Deficit Index (SMDI) and Evapotranspiration Deficit Index (ETDI) for agricultural drought monitoring. *Agricultural and Forest Meteorology*, **133**, 69-88.

Otkin, J.A., M.C. Anderson, C. Hain, and Coauthors. 2016: Assessing the evolution of soil moisture and vegetation conditions during the 2012 United States flash drought. *Agricultural and Forest Meteorology*, **218-219**, 230-242.

Pasho, E., J.J. Camarero, M. de Luis, and S.M. Vicente-Serrano. 2011: Impacts of drought at different time scales on forest growth across a wide climatic gradient in north-eastern Spain. *Agricultural and Forest Meteorology*, **151**, 1800-1811.

852 Palmer, W.C. 1965: Meteorological droughts. U.S. Department of Commerce Weather
853 Bureau Research Paper 45, 58 pp.
854 Papagiannopoulou, C., D.G. Miralles, W.A. Dorigo, N.E.C. Verhoest, M. Depoorter, and W.
855 Waegeman, W. 2017: Vegetation anomalies caused by antecedent precipitation in
856 most of the world. *Environmental Research Letters*, **12**, 074016–11.
857 Penman, H.L. 1948. Natural evaporation from open water, bare soil, and grass. *Proc. Roy.*
858 *Soc. London*, **A193**, 120–146.
859 Perdigao, J.C., R. Salgado, M.J. Costa, H.P. Dasari, A. Sanchez-Lorenzo. 2016: Variability
860 and trends of downward surface global solar radiation over the Iberian Peninsula based
861 on ERA-40 reanalysis. *International Journal of Climatology*, **36**, 3917-3933.
862 Pinzon, J.E.; and C.J. Tucker. 2014: A non-stationary 1981–2012 AVHRR NDVI3g time
863 series. *Remote Sens.*, **6**, 6929–6960.
864 Priestley, C., and R. Taylor, 1972: On the assessment of surface heat flux and evaporation
865 using large-scale parameters. *Monthly Weather Review*, **100**, 81–92.
866 Quiring, S. and T. N. Papakryiakou. 2003: An evaluation of agricultural drought indices for
867 the Canadian prairies. *Agricultural and Forest Meteorology*, **118**, 49–62.
868 Rosas, T., L. Galiano, R. Ogaya, J. Peñuelas, and J. Martínez-Vilalta. 2013: Dynamics of non-
869 structural carbohydrates in three Mediterranean woody species following long-term
870 experimental drought. *Frontiers in Plant Science*, **4**, 400,
871 http://doi.org/10.3389/fpls.2013.00400
872 Rotstayn, L.D., M.L. Roderick, and G.D. Farquhar. 2006: A simple pan-evaporation model
873 for analysis of climate simulations: Evaluation over Australia *Geophysical Research*
874 *Letters*, **33**, L17715.
875 Simelton, E., E.D.G. Fraser, M. Termansen, P.M. Forster, and A.J. Dougill. 2009: Typologies
876 of crop-drought vulnerability: an empirical analysis of the socio-economic factors that
877 influence the sensitivity and resilience to drought of three major food crops in China
878 (1961-2001). *Environmental Science and Policy*, **12**, 438-452.
879 Stagge, J.A., L.M. Tallaksen, L. Gudmundsson, A.F. Van Loon, K. Stahle. 2015: Candidate
880 distributions for climatological drought indices (SPI and SPEI). *International Journal*
881 *of Climatology,* **35**, 4027–4040.
882 Stahl, K., I. Kohn, L. De Stefano, and Coauthors. 2015: An impact perspective on pan-
883 European drought sensitivity. Drought: Research and Science-Policy Interfacing -
884 Proceedings of the International Conference on Drought: Research and Science-Policy
885 Interfacing. 329-334.
886 Stahl, K., I. Kohn, V. Blauhut, and Coauthors. 2016: Impacts of European drought events:
887 Insights from an international database of text-based reports. *Natural Hazards and*
888 *Earth System Sciences*, 16, 801-819.
889 Stephenson, N.L. 1990: Climatic control of vegetation distribution: the role of the water
890 balance. *American Naturalist*, **135**, 649-670.
891 Stephenson, N.L. 1998: Actual evapotranspiration and deficit: Biologically meaningful
892 correlates of vegetation distribution across spatial scales. *Journal of Biogeography,* **25**,
893 855-870.
894 Tucker, C.J., C. Vanpraet, E. Boerwinkel, and A. Gaston. 1983: Satellite remote sensing of
895 total dry matter production in the Senegalese Sahel. *Remote Sensing of Environment*,
896 **13**, 461–474.
897 Van Loon, A.F. 2015: Hydrological drought explained. *Wiley Interdisciplinary Reviews:*
898 *Water*, **2**, 359–392.
899 Van Loon, A.F., K. Stahl, G. Di Baldassarre, and Coauthors. 2016: Drought in a human-
900 modified world: Reframing drought definitions, understanding, and analysis
901 approaches. *Hydrology and Earth System Sciences*, **20**, 3631-3650.

902 Vicente-Serrano, S.M. 2006: Differences in spatial patterns of drought on different time
903 scales: an analysis of the Iberian Peninsula. *Water Resources Management*, **20**, 37-60.
904 Vicente-Serrano S.M., S. Beguería, J.I. López-Moreno. 2010: A Multi-scalar drought index
905 sensitive to global warming: The Standardized Precipitation Evapotranspiration Index
906 – SPEI. *Journal of Climate*, **23**, 1696-1718.
907 Vicente-Serrano, S.M., S. Beguería, J.I. López-Moreno, M. Angulo, A. El Kenawy, 2010b: A
908 new global 0.5° gridded dataset (1901-2006) of a multiscalar drought index:
909 comparison with current drought index datasets based on the Palmer Drought Severity
910 Index. *Journal of Hydrometeorology*, **11**, 1033–1043
911 Vicente-Serrano, S.M., S. Beguería and J.I. López-Moreno. 2011: Comment on
912 "Characteristics and trends in various forms of the Palmer Drought Severity Index
913 (PDSI) during 1900-2008" by A. Dai. *Journal of Geophysical Research-Atmosphere*.,
914 **116**, D19112, doi:10.1029/2011JD016410
915 Vicente-Serrano, S.M., S. Beguería, J. Lorenzo-Lacruz, and Coauthors. 2012: Performance of
916 drought indices for ecological, agricultural and hydrological applications. *Earth*
917 *Interactions*, **16**, 1–27.
918 Vicente-Serrano, S.M., J.I. López-Moreno, S. Beguería, J. Lorenzo-Lacruz, C. Azorin-
919 Molina, and E. Morán-Tejeda. 2012b: Accurate computation of a streamflow drought
920 index. *Journal of Hydrologic Engineering*, **17**, 318-332.
921 Vicente-Serrano, S.M., C. Gouveia, J.J. Camarero, and Coauthors. 2013: The response of
922 vegetation to drought time-scales across global land biomes. *Proceedings of the*
923 *National Academy of Sciences of the United States of America*, **110**, 52-57.
924 Vicente-Serrano, S.M., C. Azorin-Molina, A. Sanchez-Lorenzo, and Coauthors. 2014:
925 Reference evapotranspiration variability and trends in Spain, 1961–2011. *Global and*
926 *Planetary Change*, **121**, 26-40.
927 Vicente-Serrano, S.M., J.J. Camarero, J. Zabalza, G. Sangüesa-Barreda, J.I. López-Moreno,
928 and C.L. Tague. 2015: The evapotranspiration deficit controls growth and net primary
929 production: implications for Pyrenean silver fir growth under warmer and drier
930 conditions. *Agricultural and Forest Meteorology*, **206**, 45-54.
931 Vicente-Serrano, S.M., and S. Beguería. 2016: Comment on "Candidate Distributions for
932 Climatological Drought Indices (SPI and SPEI)" by James H. Stagge et al.
933 *International Journal of Climatology*, **36**, 2120-2131.
934 Vicente-Serrano, S.M. 2016:Foreword: Drought complexity and assessment under climate
935 change conditions. *Cuadernos de Investigación Geográfica*, **42**, 7-11.
936 Vicente-Serrano, S.M., R. Nieto, L. Gimeno, and Coauthors. 2017: Recent changes of relative
937 humidity: regional connection with land and ocean processes. *Earth System Dynamics*,
938 https://doi.org/10.5194/esd-2017-43.
939 Wang, W., W. Xing, Q Shao. 2015: How large are uncertainties in future projection of
940 reference evapotranspiration through different approaches? *Journal of Hydrology*, **524**,
941 696-700.
942 Wang, K., Z. Li, M. Cribb. 2016: Estimation of evaporative fraction from a combination of
943 day and night land surface temperatures and NDVI: A new method to determine the
944 Priestley-Taylor parameter. *Remote Sensing of Environment*, **102**, 293-305
945 Wilhite, D. A., 1993: Drought Assessment, Management and Planning: Theory and Case
946 Studies. Kluwer, 293 pp.
947 Wilhite, D.A. 2000: Drought as a natural hazard: Concepts and definitions. Drought: A
948 Global Assessment, D. Wilhite, Ed., Vol. 1, Taylor and Francis, 3–18.
949 Will, R.E., S.M. Wilson, C.B. Zou, T.C. Hennessey. 2013: Increased vapor pressure deficit
950 due to higher temperature leads to greater transpiration and faster mortality during

drought for tree seedlings common to the forest-grassland ecotone. *New Phytologist*, **200**, 366-374.

Willett, K.M., R.J.H. Dunn, P.W. Thorne, and Coauthors. 2014: HadISDH land surface multi-variable humidity and temperature record for climate monitoring. *Climate of the Past*, **10**, 1983-2006.

Yang, Y.T., R.J. Donohue, T.R. McVicar, and M.L. Roderick. 2015: An analytical model for relating global terrestrial carbon assimilation with climate and surface conditions using a rate-limitation framework. *Geophysical Research Letters*, **42**, 9825–9835.

Yang, Y.T., T.R. McVicar, R.J. Donohue, Y.Q. Zhang, M.L. Roderick, F.H.S. Chiew, F.H.S., L. Zhang and J.L. Zhang. 2017: Lags in hydrologic recovery following an extreme drought: assessing the roles of climate and catchment characteristics. *Water Resources Research*, **53**, 4821–4837.

Yao, Y., S. Liang, Q. Qin, and K. Wang, 2010: Monitoring drought over the conterminous United States using MODIS and NCEP Reanalysis-2 data. *Journal of Applied Meteorology and Climatology*, **49**, 1665–1680.

Zampieri, M., F. D'Andrea, R. Vautard, and Coauthors 2009: Hot European summers and the role of soil moisture in the propagation of mediterranean drought. *Journal of Climate*, **22**, 4747-4758.

Zhang, Y.Q., J.L. Peña-Arancibia, T.R. McVicar, F.H.S. Chiew, and Coauthors. 2016: Multi-decadal trends in global terrestrial evapotranspiration and its components. *Scientific Reports*, **6**, 19124, doi:10.1038/srep19124

Zhang, Q., D. Kong, V.P. Singh, and P. Shi. 2017: Response of vegetation to different time-scales drought across China: Spatiotemporal patterns, causes and implications. *Global and Planetary Change*, **152**, 1-11.

Zipper, S.C., J. Qiu, and C.J. Kucharik. 2016: Drought effects on US maize and soybean production: Spatiotemporal patterns and historical changes. *Environmental Research Letters*, **11**,094021.

FIGURE CAPTIONS

Figure 1: Global terrestrial relationship between SEDI (and return period - 1 event in number of cases-) obtained from GEV (a) and Pearson-III (b) distributions and log-logistic distribution using the GLEAM and CRU AED. Colors represent the density of points (dark red being the highest)

Figure 2. Percentage of series showing absolute frequencies of SEDI values below -2.58. a) GLEAM AED, b) CRU AED

Figure 3: Box and whisker plot showing the Pearson correlation coefficient (r) between SEDI series calculated from GLEAM and CRU AED the entire monthly record and for each month independently. Light Horizontal line shows the threshold for positive and significant correlations ($p < 0.05$), with numbers above the top whisker indicating the percentage of global terrestrial area with such correlations. The heavy line in the box represents the median, the upper and lower parts of the box denote the interquartile range and the whiskers show the 95% or 5%.

Figure 4: Spatial distribution of the correlations between SEDI series calculated using the GLEAM and the CRU datasets for AED for the mid-season monthly series and for the series of all months. Terrestrially white areas represent deserts/Greenland and areas in which SEDI fit has no solution

Figure 5: Spatial distribution of the SEDI values obtained from GLEAM and CRU AED data during the recent drought episodes that affected Russia (top-most three rows) and southern North America (bottom-most three rows) in 2010 and 2011, respectively.

Figure 6. Box-plot and whisker plot showing the Pearson correlation coefficient (r) between the SEDI and SPEI for specific months of the year as well as for the entire record. Light Horizontal line shows the threshold for positive and significant correlations ($p < 0.05$), with numbers above the top whisker indicating the percentage of global terrestrial area with such correlations. The heavy line in the box represents the median, the upper and lower parts of the box denote the interquartile range and the whiskers show the 95% or 5%.

Figure 7: Spatial distribution of the correlations between SEDI and SPEI series for mid-season months and for the entire record. Terrestrially white areas represent deserts/Greenland and areas in which SEDI fit has no solution.

Figure 8: Correlation between the SEDI and SPEI at different time scales (from 1- to 24-months) for specific months and for the entire record. Light Horizontal line shows the threshold for positive and significant correlations ($p < 0.05$), with numbers above the top whisker indicating the percentage of global terrestrial area with such correlations. The heavy line in the box represents the median, the upper and lower parts of the box denote the interquartile range and the whiskers show the 95% or 5%.

Figure 9. SPEI time scale at which the highest correlation with the SEDI series was found for mid-season months and for the entire record. Terrestrially white areas represent deserts/Greenland and areas in which SEDI fit has no solution.

Figure 10. Spatial distribution of the Maximum Pearson correlation coefficient (r) between SEDI and sNDVI (left) and between SPEI and sNDVI (right) for mid-season months and for the entire record 1981–2014.

Figure 11: Density scatterplots with the spatial relationship between the sNDVI and SEDI correlations and between the sNDVI and SPEI correlations. The scatterplots show the results for all months and for the entire record. Blue line: linear regression, black line: 1-to-1 line. Given the large sample, and to avoid an overrepresentation of significant correlations, the p values were obtained by means of a bootstrap sampling approach that considers 2000 independent samples of 30 cases and p values for correlations of

1029 the samples of 30 cases were averaged. The colors of the scatterplots represent the
1030 density of points (dark red being the highest).
1031 Figure 12: Spatial distribution of the SEDI, 3-month SPEI and sNDVI during two
1032 extraordinary drought events recorded in the Iberian Peninsula (1995 shown in the top-
1033 three rows) and the Sahel (1984 shown in the bottom three rows).
1034

Table 1: Percentage of monthly time series of ED with no fitting solution tested with the eight probability distributions.

Month	Log-logistic		GEV		Log-normal		Pearson-III		Weibull		G. Pareto		Normal		Exponential	
	GLEAM	CRU	GLEAM	CRU	GLEAM	CRU	GLEAM	CRU	GLEAM	CRU	GLEAM	CRU	GLEAM	CRU	GLEAM	CRU
Jan.	34.6	15.4	34.6	15.4	77.9	68.8	34.6	15.4	62.4	38.3	34.6	15.4	31.6	12.9	31.6	12.9
Feb.	13.9	2.9	13.9	2.9	74.5	67.9	13.9	2.9	49.4	30.5	13.9	2.9	12.1	1.8	12.1	1.8
Mar.	5.2	1.9	5.2	1.9	63.9	66.7	5.2	1.9	34.2	22.9	5.2	1.9	4.8	1.6	4.8	1.6
Apr.	2.5	0.4	2.5	0.4	58.0	63.7	2.5	0.4	29.5	17.7	2.5	0.4	2.2	0.3	2.2	0.3
May	0.4	0.3	0.4	0.3	59.9	57.3	0.4	0.3	27.8	11.7	0.4	0.3	0.4	0.2	0.4	0.2
Jun.	0.7	0.9	0.7	0.9	66.6	58.1	0.7	0.9	35.0	12.6	0.7	0.9	0.7	0.7	0.7	0.7
Jul.	0.6	0.8	0.6	0.8	69.6	60.6	0.6	0.8	40.6	15.6	0.6	0.8	0.5	0.6	0.5	0.6
Aug.	1.6	0.3	1.6	0.3	69.7	61.0	1.6	0.3	46.7	15.9	1.6	0.3	1.4	0.2	1.4	0.2
Sep.	4.4	0.3	4.4	0.3	68.9	56.9	4.4	0.3	46.9	10.6	4.4	0.3	4.2	0.2	4.2	0.2
Oct.	19.2	0.8	19.2	0.8	72.1	57.0	19.2	0.8	49.9	17.7	19.2	0.8	18.4	0.4	18.4	0.4
Nov.	37.6	5.8	37.6	5.8	77.7	66.3	37.6	5.8	61.0	30.8	37.6	5.8	36.2	4.4	36.2	4.4
Dec.	43.3	13.7	43.3	13.7	81.3	68.0	43.3	13.7	67.2	38.9	43.3	13.7	41.6	10.1	41.6	10.1

Table 2: Percentage of monthly SEDI series calculated using the remaining six probability distributions for which the null hypothesis of normality was rejected (fail-to-reject-rate) by the Shapiro-Wilks test at a confidence level p = 0.05.

Month	Log-logistic		GEV		Pearson-III		G. Pareto		Normal		Exponential	
	GLEAM	CRU	GLEAM	CRU	GLEAM	CRU	GLEAM	CRU	GLEAM	CRU	GLEAM	CRU
Jan.	75.9	60.0	68.0	58.6	65.7	58.2	20.4	13.1	35.5	46.6	11.2	8.2
Feb.	74.3	57.6	68.7	57.1	66.6	56.7	22.4	14.7	38.8	46.7	10.7	8.8
Mar.	86.3	66.3	79.4	64.4	77.0	65.2	24.0	14.3	50.3	53.4	14.4	9.2
Apr.	89.0	78.1	81.3	74.2	79.3	74.6	22.6	15.4	51.3	59.3	16.1	10.2
May	91.4	88.7	83.2	85.5	80.8	86.1	23.6	18.0	51.3	71.5	15.2	12.0
Jun.	92.8	89.1	81.6	85.5	79.9	86.3	19.5	18.9	48.2	71.9	11.8	12.0
Jul.	91.4	88.9	80.8	84.9	78.5	86.2	19.1	18.5	44.2	71.3	10.6	11.1
Aug.	87.7	88.8	75.8	85.1	72.1	86.0	17.9	17.7	36.5	68.1	11.2	11.0
Sep.	87.3	88.7	73.9	85.4	70.7	86.0	20.4	17.9	36.6	71.5	12.3	11.7
Oct.	83.6	72.3	72.8	70.8	70.2	70.6	19.2	17.9	38.1	58.0	12.5	11.1
Nov.	81.8	59.0	73.3	56.8	71.1	56.5	20.1	11.9	40.9	46.5	12.8	7.4
Dec.	76.9	53.4	68.2	52.4	66.4	51.8	18.3	12.6	37.7	40.2	10.8	7.6

1045 Table 3: Percentage of global terrestrial 0.5°-degree resolution grid points at which the maximum
1046 correlation between the SEDI and SPEI is recorded corresponding to different SPEI time scales.

SPEI Time scale (months)	All months	Jan.	Feb.	Mar.	Apr.	May	Jun.	Jul.	Aug.	Sep.	Oct.	Nov.	Dec.
1	42.0	21.5	24.5	31.9	40.7	42.0	42.0	38.0	32.9	33.5	23.4	24.5	20.2
2	20.2	14.9	13.5	14.6	14.3	14.7	13.9	17.6	17.9	14.9	17.1	19.2	17.8
3	9.7	11.9	8.2	10.1	8.5	8.3	9.4	7.6	9.8	9.6	9.3	12.1	13.1
4	7.5	7.8	8.6	6.7	6.6	4.5	6.0	6.4	6.9	7.1	7.8	5.8	7.5
5	4.3	5.2	5.3	5.1	4.5	4.2	3.6	4.5	4.7	4.3	6.3	4.9	5.8
6	3.7	4.8	4.6	5.1	2.7	3.2	3.0	3.5	3.6	3.6	4.1	4.2	4.0
7	2.3	3.1	4.2	3.8	3.0	3.1	2.4	2.6	2.3	2.7	2.9	3.3	3.4
8	1.9	3.5	2.9	2.8	2.4	2.8	2.7	2.3	1.8	1.8	2.5	3.6	2.7
9	1.3	2.1	4.4	2.6	1.8	2.4	2.2	2.1	1.7	1.4	1.5	1.8	3.4
10	1.1	2.0	2.5	1.4	2.2	2.7	2.4	1.8	1.7	1.9	1.9	1.7	2.5
11	0.7	1.6	2.0	1.5	1.6	1.5	1.6	2.3	1.6	1.7	1.2	1.6	1.7
12	0.5	1.5	1.2	1.5	1.3	1.1	1.3	1.8	2.7	1.9	1.3	1.5	1.2
13	0.3	1.1	0.8	0.8	0.8	0.8	0.8	0.8	1.5	1.3	1.4	0.9	1.0
14	0.2	1.1	0.9	0.6	0.6	0.5	0.8	0.9	1.6	1.9	1.6	1.0	1.0
15	0.3	1.3	1.2	0.8	0.5	0.4	0.8	0.7	1.3	1.6	1.7	1.3	1.2
16	0.3	2.0	1.3	0.8	0.6	0.5	0.5	0.7	0.8	1.2	2.1	1.0	1.0
17	0.3	1.5	1.0	0.6	0.6	0.5	0.6	0.5	0.7	1.0	2.1	1.5	1.2
18	0.1	1.9	1.0	0.9	0.6	0.5	0.6	0.5	0.6	0.9	1.1	1.6	1.6
19	0.4	1.4	2.2	0.7	0.7	0.5	0.7	0.5	0.4	0.6	1.0	1.1	1.6
20	0.5	1.5	1.6	1.1	1.2	0.8	0.6	0.7	0.6	0.5	1.0	1.3	1.3
21	0.4	1.9	1.8	1.6	0.9	1.1	0.6	0.6	0.8	1.0	0.7	1.0	1.4
22	0.4	1.6	1.7	1.4	0.6	0.8	0.9	0.7	0.7	1.1	1.4	1.1	1.2
23	0.5	1.5	1.4	1.1	1.0	1.2	1.1	1.0	1.1	1.6	2.9	1.2	1.7
24	1.3	3.7	3.0	2.8	2.3	1.8	1.6	2.1	2.5	2.8	3.7	2.9	2.8

1047

1048

1049 Table 4. Percentage of the global terrestrial areas showing significant correlations between sNDVI
1050 and SEDI and between sNDVI and SPEI

1051

1052

1053

1054

	sNDVI vs. SEDI	sNDVI vs. SPEI
All months	13.09	19.24
January	23.52	36.94
February	22.74	35.68
March	23.59	37.12
April	26.67	38.08
May	27.81	37.63
June	24.49	41.22
July	26.84	43.88
August	26.21	46.72
September	23.95	43.67
October	25.35	42.92
November	25.41	37.64
December	28.93	39.10

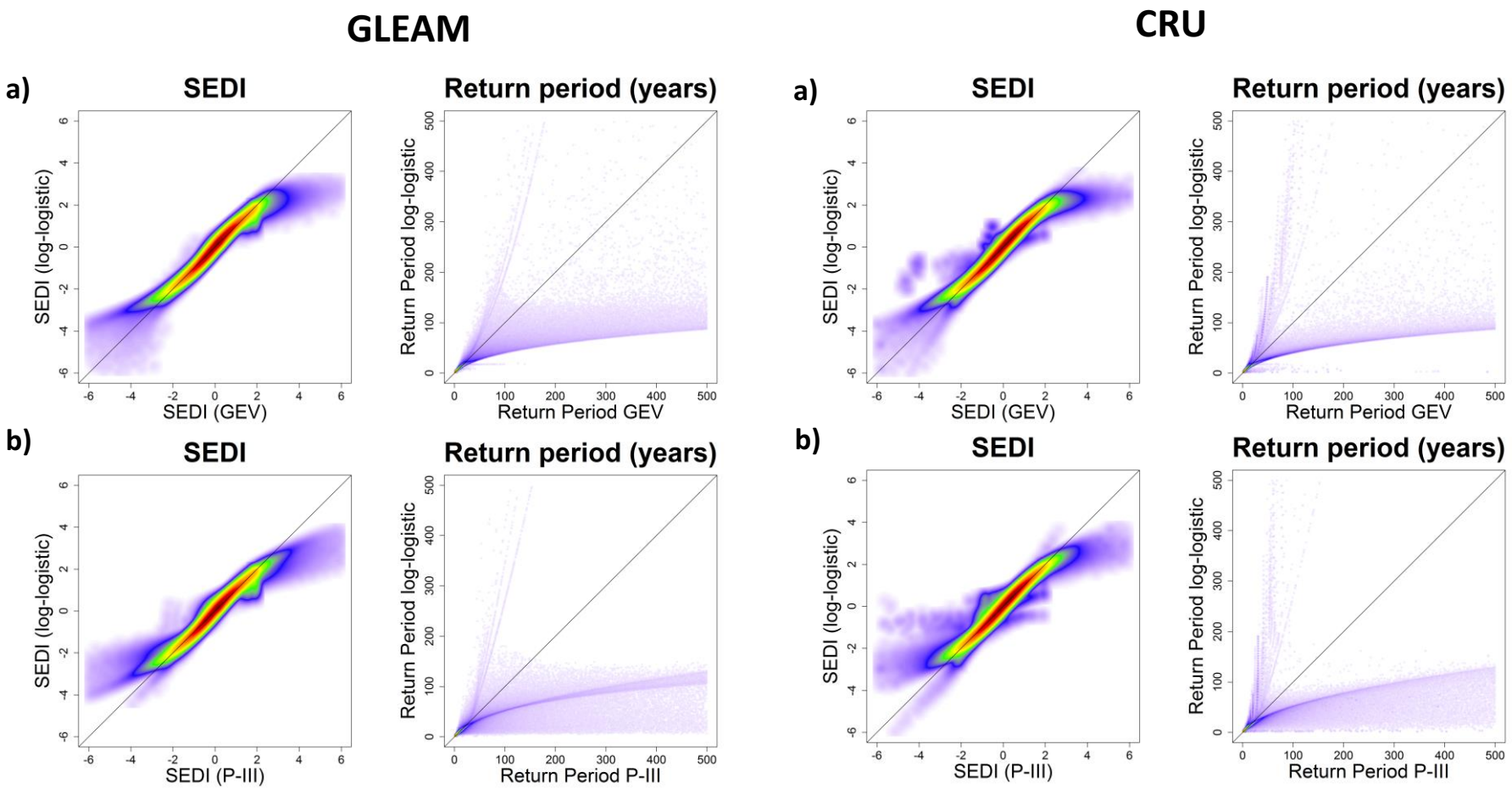

Figure 1: Global terrestrial relationship between SEDI (and return period - 1 event in number of cases-) obtained from GEV (a) and Pearson-III (b) distributions and log-logistic distribution using the GLEAM and CRU AED. Colors represent the density of points (dark red being the highest)

1059

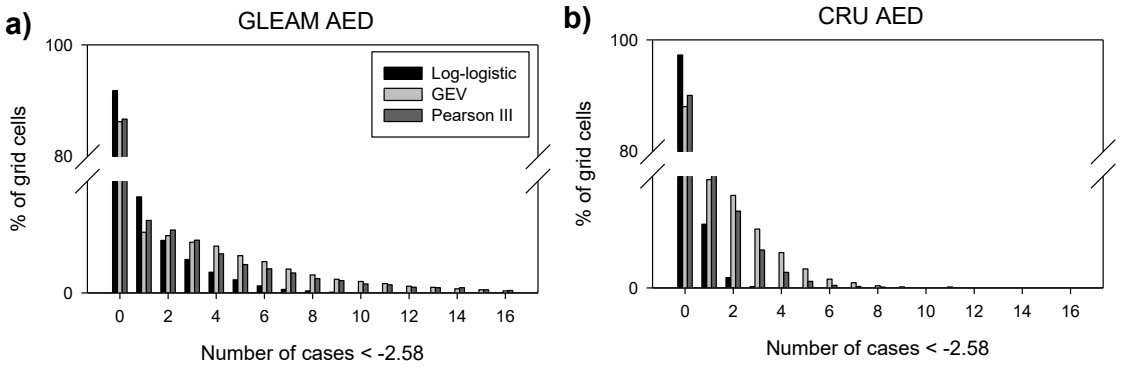

1060

1061 Figure 2. Percentage of series showing absolute frequencies of SEDI values below -2.58. a)
1062 GLEAM AED, b) CRU AED

1063

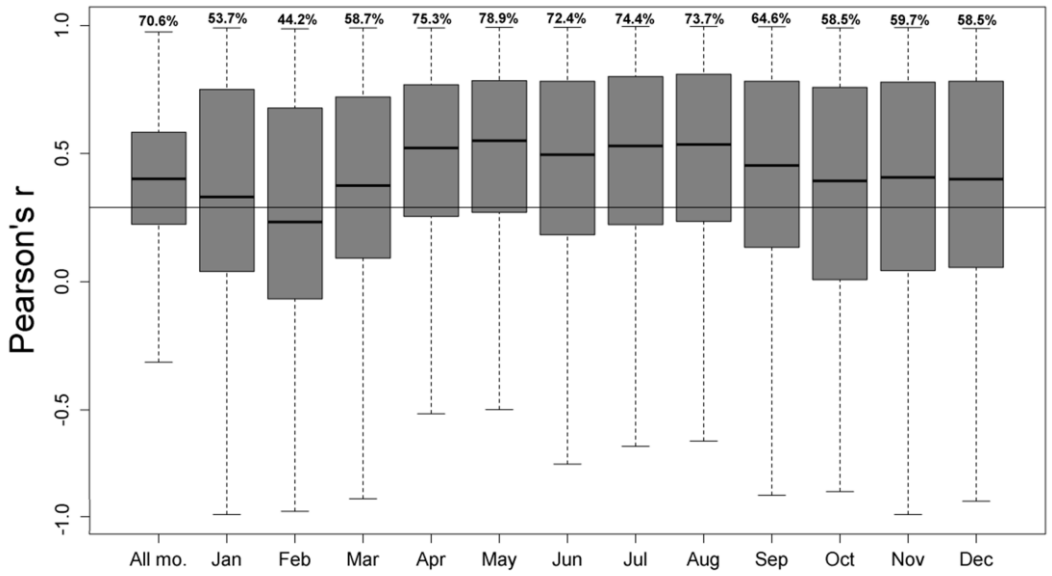

Figure 3: Box and whisker plot showing the Pearson correlation coefficient (*r*) between SEDI series calculated from GLEAM and CRU AED the entire monthly record and for each month independently. Light Horizontal line shows the threshold for positive and significant correlations ($p < 0.05$), with numbers above the top whisker indicating the percentage of global terrestrial area with such correlations. The heavy line in the box represents the median, the upper and lower parts of the box denote the interquartile range and the whiskers show the 95% or 5%.

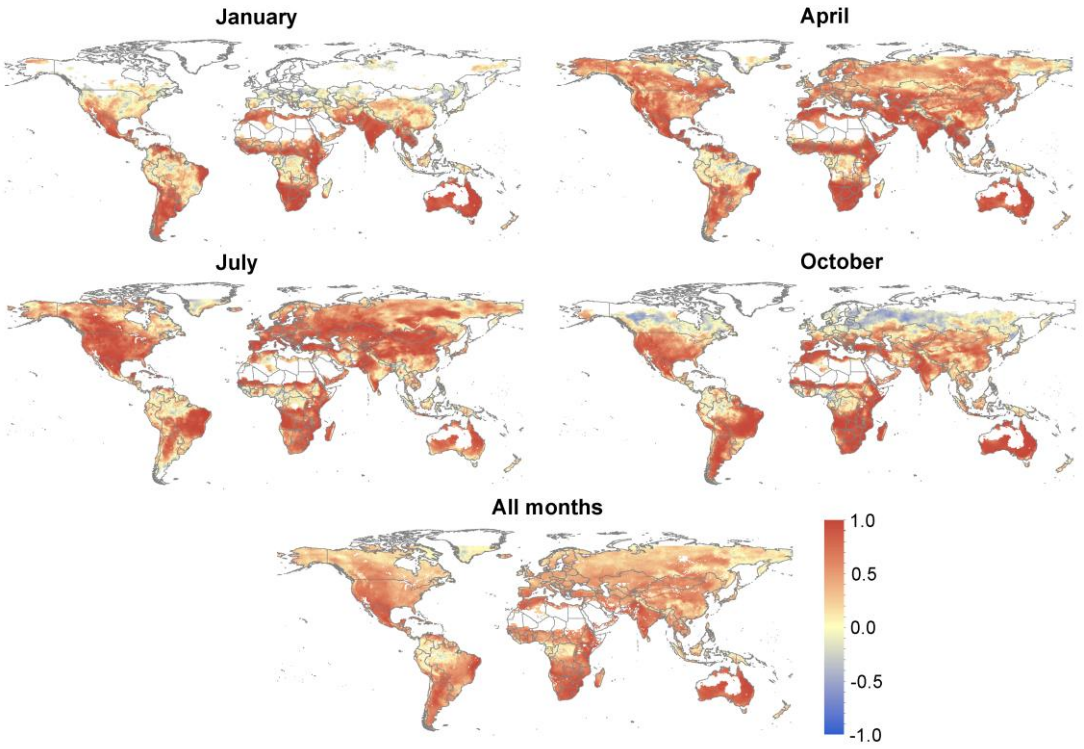

Figure 4: Spatial distribution of the correlations between SEDI series calculated using the GLEAM and the CRU datasets for AED for the mid-season monthly series and for the series of all months. Terrestrially white areas represent deserts/Greenland and areas in which SEDI fit has no solution

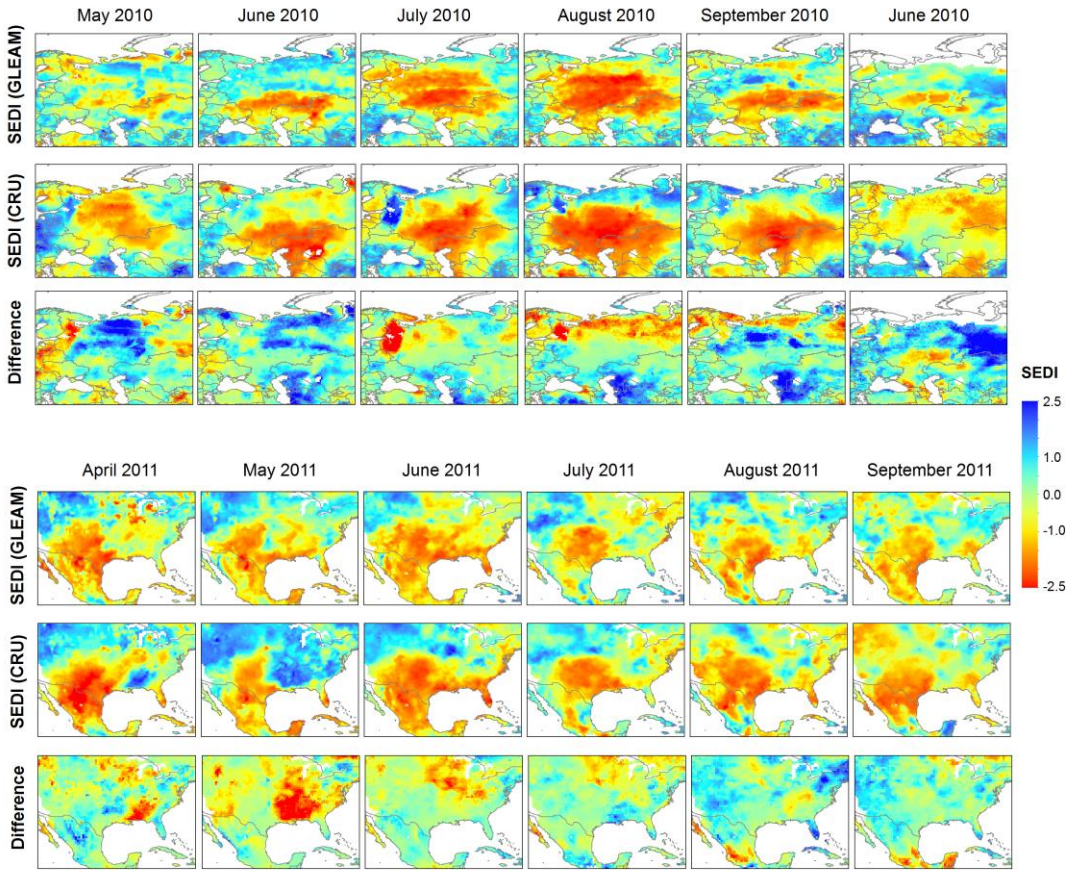

Figure 5: Spatial distribution of the SEDI values obtained from GLEAM and CRU AED data during the recent drought episodes that affected Russia (top-most three rows) and southern North America (bottom-most three rows) in 2010 and 2011, respectively.

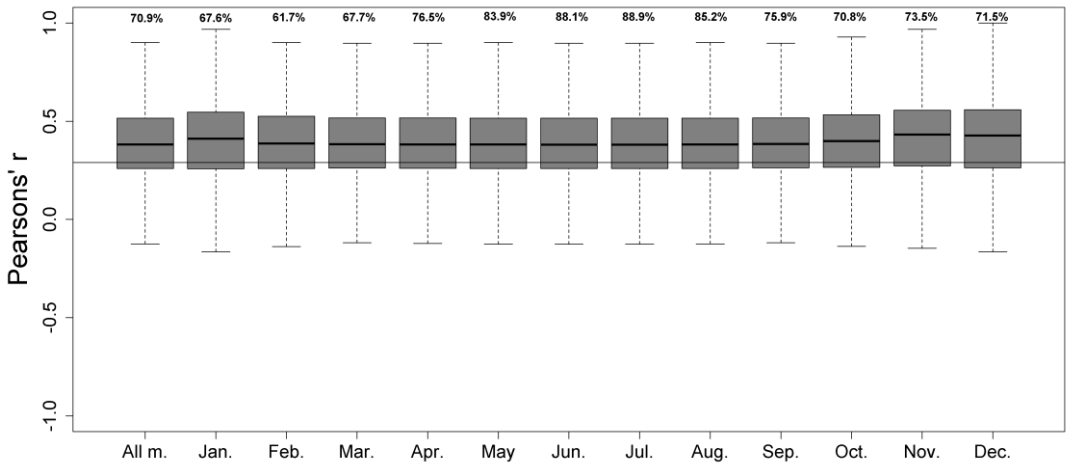

Figure 6. Box-plot and whisker plot showing the Pearson correlation coefficient (*r*) between the SEDI and SPEI for specific months of the year as well as for the entire record. Light Horizontal line shows the threshold for positive and significant correlations ($p < 0.05$), with numbers above the top whisker indicating the percentage of global terrestrial area with such correlations. The heavy line in the box represents the median, the upper and lower parts of the box denote the interquartile range and the whiskers show the 95% or 5%.

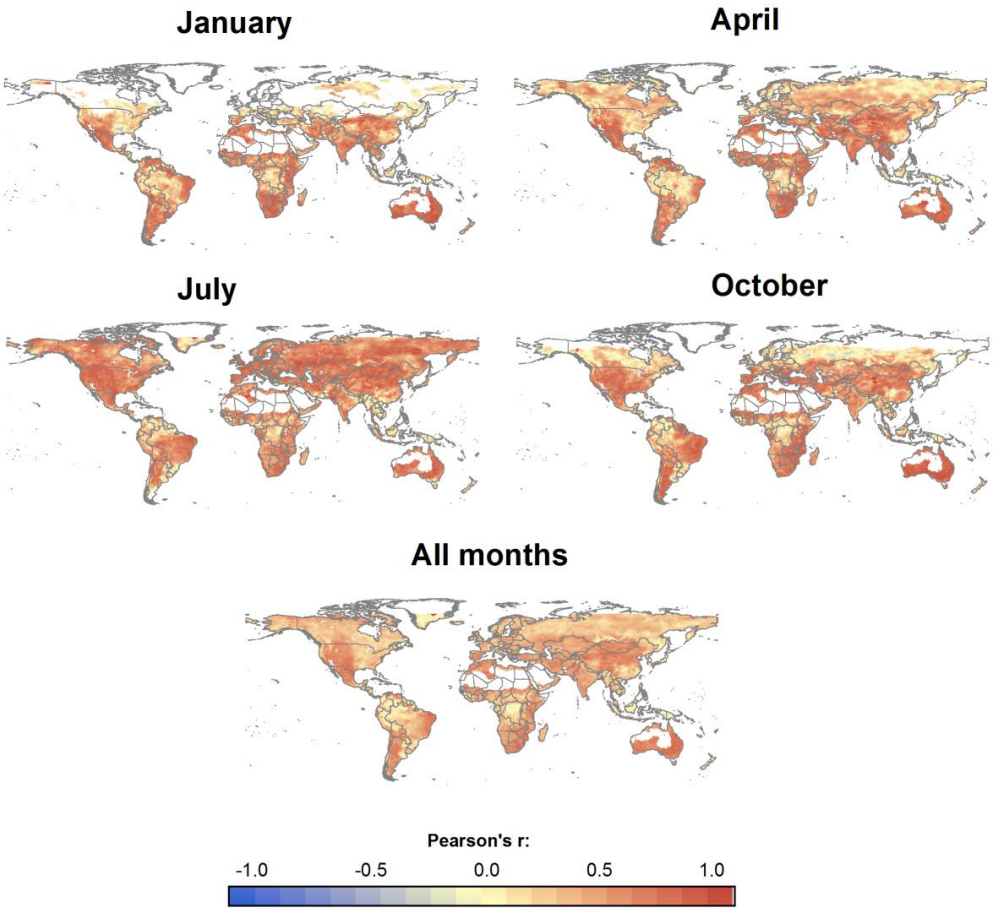

Figure 7: Spatial distribution of the correlations between SEDI and SPEI series for mid-season months and for the entire record. Terrestrially white areas represent deserts/Greenland and areas in which SEDI fit has no solution.

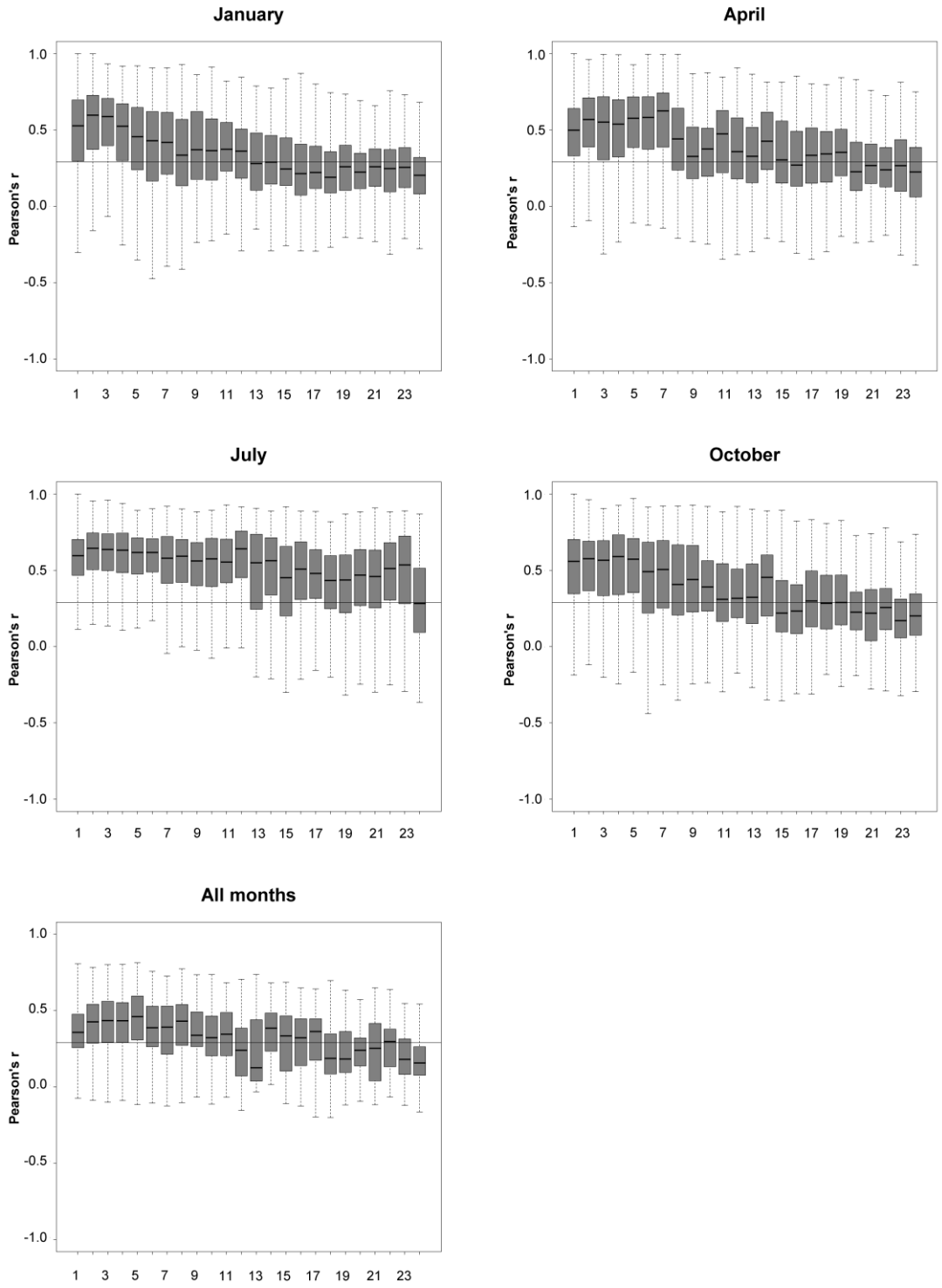

Figure 8: Correlation between the SEDI and SPEI at different time scales (from 1- to 24-months) for specific months and for the entire record. Light Horizontal line shows the threshold for positive and significant correlations ($p < 0.05$), with numbers above the top whisker indicating the percentage of global terrestrial area with such correlations. The heavy line in the box represents the median, the upper and lower parts of the box denote the interquartile range and the whiskers show the 95% or 5%.

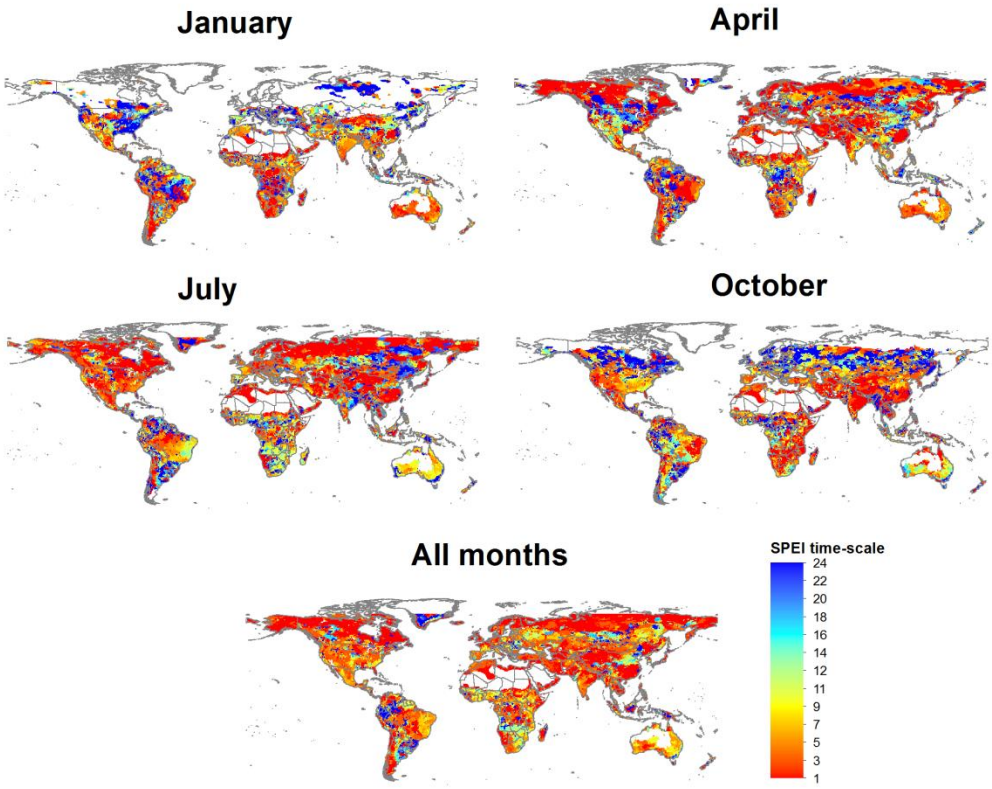

Figure 9. SPEI time scale at which the highest correlation with the SEDI series was found for mid-season months and for the entire record. Terrestrially white areas represent deserts/Greenland and areas in which SEDI fit has no solution.

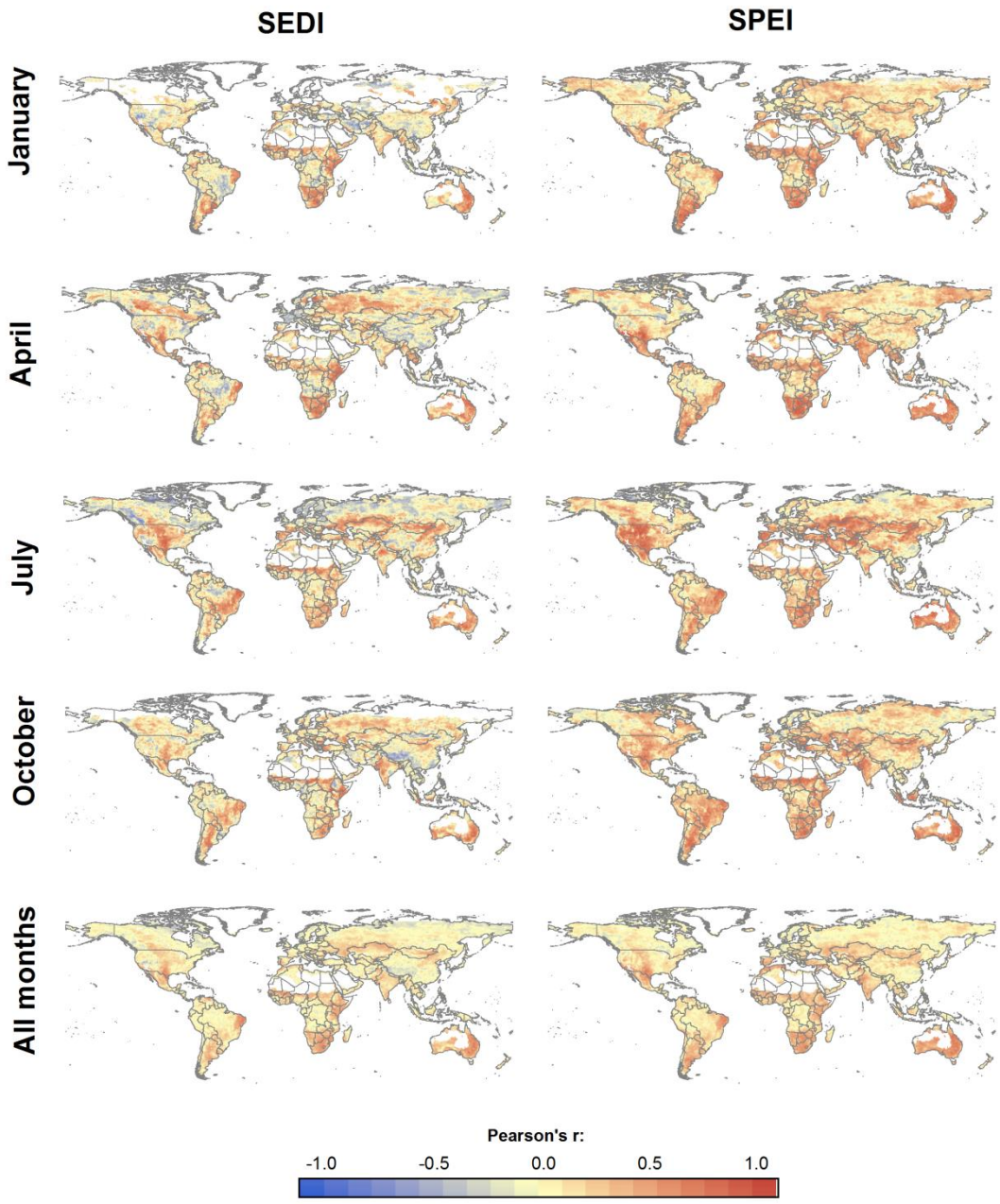

Figure 10. Spatial distribution of the Maximum Pearson correlation coefficient (*r*) between SEDI and sNDVI (left) and between SPEI and sNDVI (right) for mid-season months and for the entire record 1981–2014.

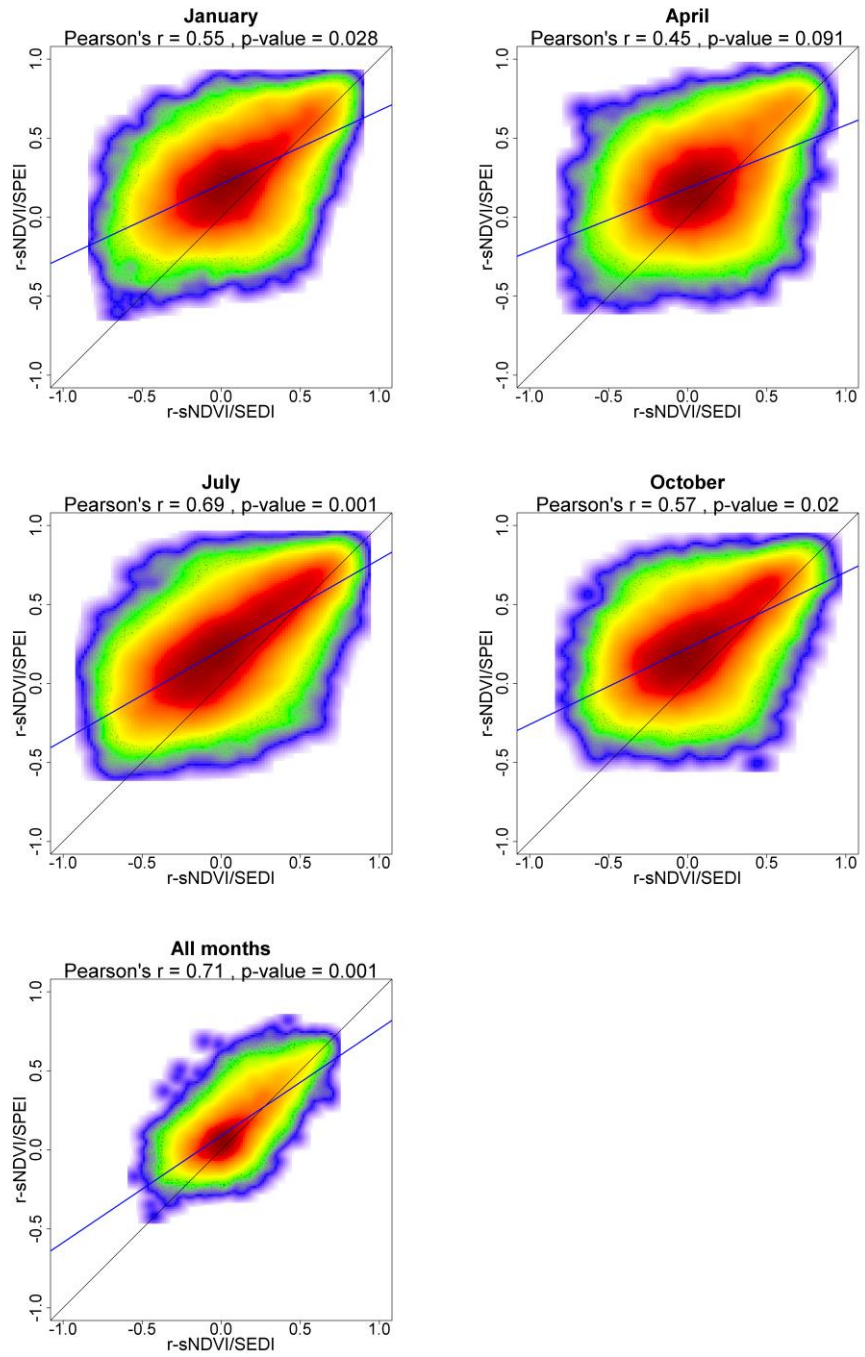

Figure 11: Density scatterplots with the spatial relationship between the sNDVI and SEDI correlations and between the sNDVI and SPEI correlations. The scatterplots show the results for all months and for the entire record. Blue line: linear regression, black line: 1-to-1 line. Given the large sample, and to avoid an overrepresentation of significant correlations, the *p* values were obtained by means of a bootstrap sampling approach that considers 2000 independent samples of 30 cases and *p* values for correlations of the samples of 30 cases were averaged. The colors of the scatterplots represent the density of points (dark red being the highest).

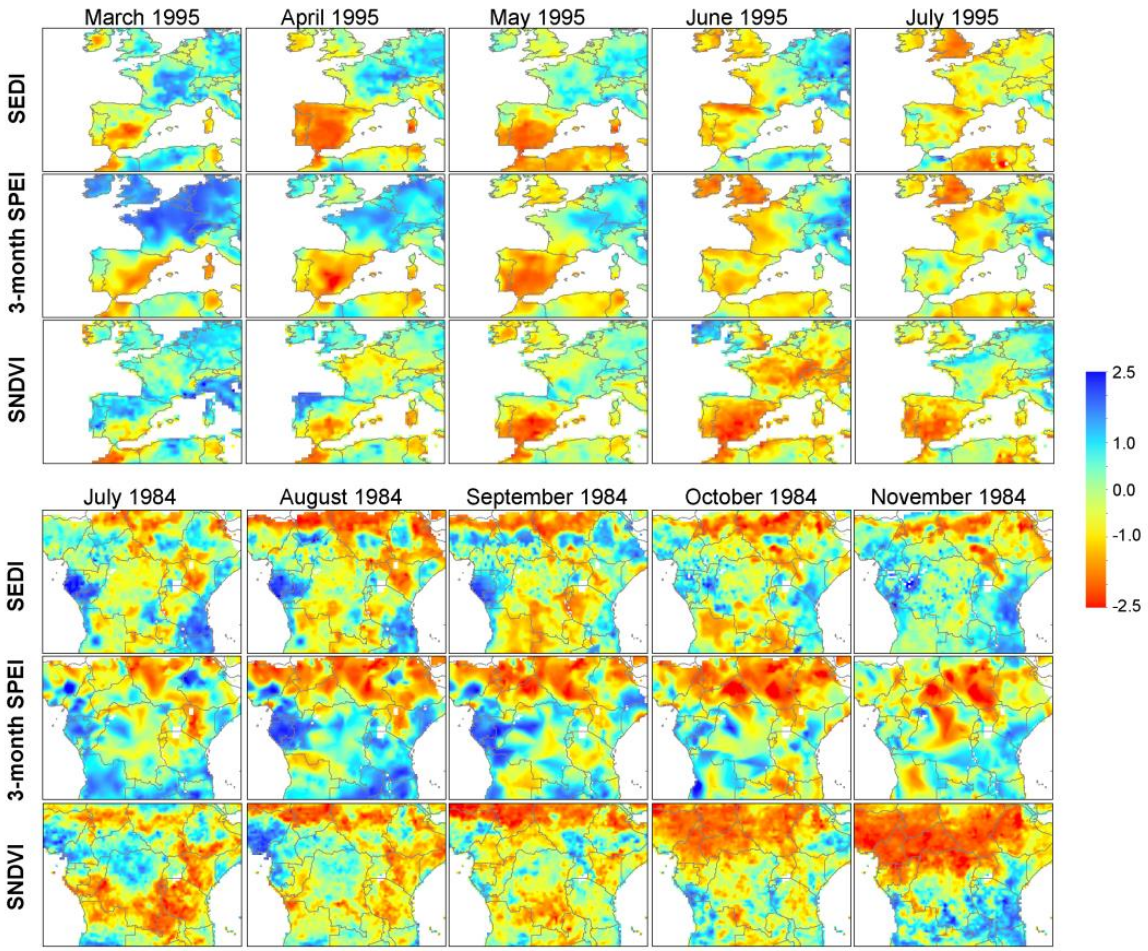

Figure 12: Spatial distribution of the SEDI, 3-month SPEI and sNDVI during two extraordinary drought events recorded in the Iberian Peninsula (1995 shown in the top-three rows) and the Sahel (1984 shown in the bottom three rows).